NORGES TEKNISK-NATURVITENSKAPELIGE UNIVERSITET

Stochastic model for fault geometry conditioned to seismic data and well observations

by

Hilde G. Borgos, Henning Omre and Chris Townsend

PREPRINT
STATISTICS NO. 5/2000

NORWEGIAN UNIVERSITY OF SCIENCE AND TECHNOLOGY
TRONDHEIM, NORWAY

This report has URL http://www.math.ntnu.no/preprint/statistics/2000/S5-2000.ps
Hilde G. Borgos has homepage: http://www.math.ntnu.no/~hgb
E-mail: hgb@stat.ntnu.no
Address: Department of Mathematical Sciences, Norwegian University of Science and Technology, N-7491 Trondheim, Norway.

Stochastic model for fault geometry conditioned to seismic data and well observations

Hilde G. Borgos[1], Henning Omre[1] and Chris Townsend[2]

[1] Department of Mathematical Sciences, NTNU, Trondheim, Norway.
[2] Statoil Research Centre, Trondheim, Norway.

Abstract

A Bayesian framework is used to define a stochastic model of fault patterns conditioned to seismic data and well data. Faults above seismic resolution are considered, enabling assessment of uncertainty for faults detectable from seismic data. The fault pattern is represented through a faulted horizon, with a prior distribution modeling characteristics of fault traces, fault intersections and offset profiles. A likelihood function is defined under the assumption that reflection coefficients of a non-faulted, layered sedimentary reservoir can be modeled as a Gaussian random field with a strong horizontal correlation. Uncertainty in fault patterns is studied through repeated sampling from the posterior distribution.

1 Introduction

Geological faults above seismic resolution can be interpreted from seismic reflection data. Sedimentary rocks tend to form horizontally layered sequences. This layered structure is often observed in the seismic data, where lateral discontinuities visible across succeeding horizontal layers are interpreted as faults. However, the interpretations of faults from seismic data contain uncertainties, both due to the seismic data quality, seismic resolution and the judgment of the interpreter. Furthermore, the subjective human interpretations are not always guaranteed to give geologically realistic fault patterns, especially if the interpreter is poorly trained or has a particular bias. Another problem related to interpreting seismic maps, is the problem of matching faults interpreted from succeeding two dimensional maps to create a three dimensional fault pattern. Badley et al. (1990) discuss a methodology for interpreting faults from three dimensional seismic data.

Attempts have been made to create algorithms for detecting faults from three dimensional (3D) seismic data. Bahorich and Farmer (1995) introduce a successful technique (the

Coherence Cube) for tracking/highlighting faults from 3D seismic data. The method is essentially a moving window correlation algorithm, and is patented, see Bahorich and Farmer (1996). Further developments based on the idea behind the Coherence Cube are presented by Marfurt et al. (1998) and Marfurt et al. (1999). Two alternative techniques for detecting faults and stratigraphic boundaries from 3D seismic data are described by Luo et al. (1996). The techniques presented in the cited papers are deterministic procedures used at an early stage in the interpretation process, and thus making the interpretation easier and faster. The techniques give indications of fault positions, lengths, connectivity and orientations. Experience and use of these techniques have shown that they neither improve fault resolution, nor do they significantly reduce uncertainty. They also tend to be prone to seismic noise and only have a real benefit if used at an early stage.

In this work, the problem of detecting faults from 3D seismic data is considered from a statistical point of view. The method is both novel and clearly different from the previously mentioned correlation techniques. A stochastic model for post-sedimentary fault patterns is defined, conditioned to 3D seismic data and well observations. The layered structure observed in seismic data is incorporated in the model, and the aim is to locate faults based on discontinuities in the lateral consistency. Additional information about the reservoir obtained from wells are also included in the model. Furthermore, general geological knowledge of faults and fault patterns are incorporated in the model in an attempt to produce geologically realistic fault patterns.

Previous work on stochastic modeling of faults and fractures include both pixel or grid based approaches, see for example Gringarten (1996, 1998), object based models, e.g., Chilès (1988), Brand and Haldorsen (1988), Gauthier and Lake (1993), Munthe et al. (1993), Munthe et al. (1994), Wen and Sinding-Larsen (1997), and one dimensional models where faults or fractures only appear as points, see Belfield (1998). Some of the cited papers include information from observations. Fault or fracture observations in wells are conditioned to in some cases, while often data is only used to estimate parameters related to characteristics of faults and fault patterns. For example, seismic data or outcrop data are used to estimate distributions of fault size or orientation, and spatial fault densities. Previous stochastic modeling of faults based on seismic observations mainly use interpreted seismic data to model sub-seismic fault patterns. In contrast, the stochastic model described here is defined for faults at seismic scales, and is used to assess uncertainty in the fault pattern at these scales.

A Bayesian framework is used to present the stochastic model for fault patterns, and to condition to available information like seismic data and well observations. For previous work using a Bayesian framework in reservoir modeling, see for example Lia et al. (1997), Omre and Tjelmeland (1997), Eide et al. (1997a), Eide et al. (1997b), Eide (1999). In this work the focus is on the network of faults in the reservoir. The relationship between specific reservoir characteristics and the available observations is integrated in the model, enabling conditioning of fault patterns to the observations. General geological knowledge is incorporated in a prior distribution, while the available observations are integrated in the model through the likelihood function. The posterior distribution combines the general knowledge and the observations. Assessment of uncertainty of fault geometries can be based on repeated sampling from the posterior model.

Both the prior model and the likelihood function presented in this work are defined using random fields: Markov Random Fields and Gaussian Random Fields, see Cressie (1993), Tjelmeland (1996), Abrahamsen (1997).

2 Bayesian Framework

A stochastic model is defined for a faulted horizon H, a topographic surface embedded in three dimensions. Faults, their positions, orientations and displacements, are visible as discontinuities in the surface. Let $\boldsymbol{O}$ denote available observations obtained from the reservoir under study, consisting of seismic data and well observations. The aim of this work is to generate geological fault patterns, represented by faulted horizons H, conditioned on the available observations $\boldsymbol{O}$. A Bayesian framework is used to define the relationship between the faulted horizon and the observations. A prior model $f(h)$ of the faulted horizon includes general geological knowledge about faults and fault patterns, and is discussed in Section 3. The relationship between the faulted horizon and the observations is defined through the likelihood function $f(\boldsymbol{o}|h)$, discussed in Section 4. Combining the prior distribution and the likelihood function, the posterior distribution is obtained:

$$f(h|\boldsymbol{o}) = \text{const} \times f(h)f(\boldsymbol{o}|h). \tag{1}$$

The posterior distribution combines general geological knowledge and reservoir specific observations and is discussed in Section 5. Sampling from the posterior distribution is described in Section 6.

Some basic model assumptions are made. The vertical extents of the faults are assumed to be large compared to the vertical extent of the region under study, thus vertically all faults penetrate completely through the region. Furthermore a crude approximation is made, assuming that faults within the region has a vertical dip and a constant offset vertically.

3 Prior Model of Geological Fault Patterns

Post sedimentary faults are studied in this work. Consider a layered rock where all layers originally are horizontal, as is often the case for sedimentary rocks. This corresponds to the fundamental geological principle that sedimentary rocks are deposited horizontally, see Monroe and Wicander (1994, chap. 17). When post sedimentary faults emerge through the rock volume, rock in different parts of a layer are displaced with different offsets, and an originally horizontal surface is deformed into a topographic surface embedded in three dimensions, denoted a horizon.

Faults form brittle, discrete deformation in sedimentary strata. Other types of deformation, like ductile deformation, folding and tilting, are in this work assumed to be relatively small and are modeled as natural variations in the topographic surface. Thus the variations in the horizon are composed of displacements caused by faulting and other natural variations.

When numerous faults are present in an area, a fault pattern is created. A fault pattern is usually best observed by examining a single horizon from above, i.e., a topographic map. However, the total three dimensional extent of the faults can not be obtained from the surface, and only the pattern of fault traces on the horizon can be mapped. Fault traces are the intersections of fault planes with the horizon. The fault pattern can be represented through the number of faults, their position, geometry, displacement and displacement direction.

Under the model assumptions outlined in Section 2, a series of overlying horizons will have similar topographies, and the fault pattern can be represented through a single representative horizon H. The prior model of the geological fault pattern is defined through the probability density function (pdf) $f(h)$ of the faulted horizon H, and should contain general geological knowledge about faults and fault patterns. In Section 3.1 the faulted horizon is parameterized by an image, and in Section 3.2 a prior model of the image is defined.

3.1 Faulted horizon

A fault pattern is represented by the topography of a faulted horizon H, where faults are recognized as discontinuities in the surface. The number of faults, their position and the offsets are found from these discontinuities. The faulted horizon is parameterized by an image, where both pixels, edges and vertices are included in the model. Figure 1 gives an illustration of two types of pixels and the corresponding edges and vertices.

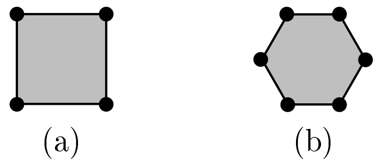

Figure 1: (a) Square pixel and (b) hexagonal pixel. The pixels are colored gray, the edges around the pixel are marked with solid lines and the vertices with circles.

Edges form an image of fault traces on a horizon. Each edge E is assigned a value in the set $\Omega_e = \{0, 1\}$, and fault traces are composed of connected edges of values $E = 1$.

Vertices represent the offsets along fault traces. Vertices V along connected edges of values $E = 1$ are assigned a value corresponding to the offset of the fault at the point of the vertex. A vertex takes a value in the set $\Omega_v \subseteq \mathbb{R}$, where the sign of the offset indicates the offset direction. Vertices connecting only edges of value $E = 0$ is assigned zero offset $V = 0$.

Pixels represent the topography of the faulted horizon, consisting of displacements caused by faulting and other natural variations. The value of a pixel P determines the altitude of the surface in the center point of the pixel. Each pixel is assigned a value from the set $\Omega_p \subseteq \mathbb{R}$.

Let $\mathcal{E}$, $\mathcal{V}$ and $\mathcal{P}$ denote the index sets of edges, vertices and pixels respectively, and let $n_e = |\mathcal{E}|$, $n_v = |\mathcal{V}|$ and $n_p = |\mathcal{P}|$ be the number of edges, vertices and pixels. The edge values are given by the vector $\boldsymbol{E} = \{E_i;\, i \in \mathcal{E}\}$, the vertices by $\boldsymbol{V} = \{V_i;\, i \in \mathcal{V}\}$ and the pixels by $\boldsymbol{P} = \{P_i;\, i \in \mathcal{P}\}$. All edges E_i, vertices V_i and pixels P_i are treated as stochastic variables, and the sample space of the image $(\boldsymbol{E}, \boldsymbol{V}, \boldsymbol{P})$ is given by $\Omega = \Omega_e^{n_e} \times \Omega_v^{n_v} \times \Omega_p^{n_p}$.

A hexagonal grid is used to represent the image, as was used by Besag (1989) and Tjelmeland and Besag (1998). An example of a hexagonal grid is given in Figure 2. The main advantage of a hexagonal grid, compared to a square grid, is that it gives a greater flexibility in drawing angles of different sizes between fault traces.

The number of pixels, edges and vertices are easily found in the hexagonal grid. Let r be the number of pixels along one side of the hexagonal grid. This is equal to the number of concentric hexagonal bands of pixels included in the grid, starting with the center pixel as band number one. The total number of pixels, edges and vertices in the grid is $n_p = 3r(r-1) + 1$, $n_e = 3r(3r-1)$ and $n_v = 6r^2$ respectively.

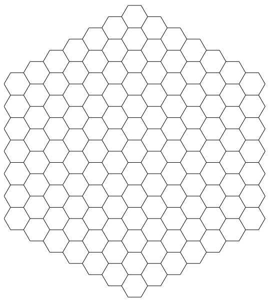

Figure 2: The image $(\boldsymbol{E}, \boldsymbol{V}, \boldsymbol{P})$ is represented by a hexagonal grid.

The image composed of the variables $(\boldsymbol{E}, \boldsymbol{V}, \boldsymbol{P})$ gives a discrete parameterization of the topography of the faulted horizon. A continuous representation of the horizon is obtained by triangulation between pixels, where faults are represented as discontinuities in the triangulation surface. The triangulation is uniquely determined by the stochastic variables $(\boldsymbol{E}, \boldsymbol{V}, \boldsymbol{P})$. The resulting topographic surface is also stochastic, and is denoted $H = H(\boldsymbol{E}, \boldsymbol{V}, \boldsymbol{P})$. The altitude of the surface H at a point (x, y) is given by $H(x, y)$. At the center point (x, y) of any pixel, with value $P = p$, the altitude of the surface equals the value of the pixel, $H(x, y) = p$.

The first step in the triangulation is to draw triangles between the center points of the pixels, as shown in Figure 3. Each side of a triangle crosses an edge in the image. If one or more of the edges have value $E = 1$, a fault intersects the triangle. The triangle is then divided into smaller triangles in order to obtain a discontinuity along the fault trace, as shown in Figure 4. In this way the image is covered by triangles, where the surface $H(x, y)$ is continuous within each triangle, and discontinuities in the surface are all located along triangle sides. An example of a topographic surface, found by triangulation from an image $(\boldsymbol{E}, \boldsymbol{V}, \boldsymbol{P})$, is shown in perspective in Figure 5.

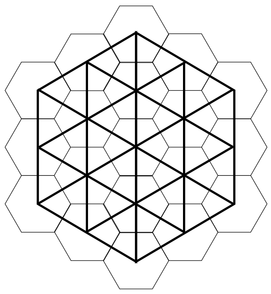

Figure 3: As a first step in the triangulation, triangles are drawn between the center points of the pixels.

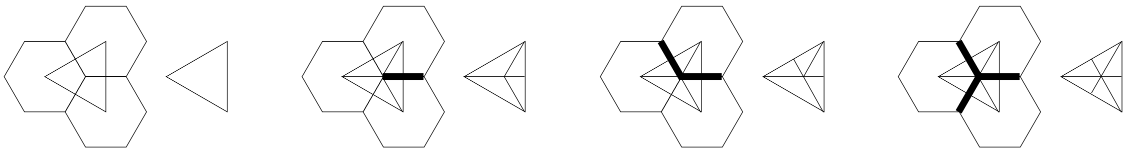

(a) (b) (c) (d)

Figure 4: Subdivisions of the triangles shown in Figure 3. The pixels are shown to the left in each figure, and edges of value $E = 1$ are marked with thick solid lines. The subdivisions of the triangle are illustrated to the right. (a) If no faults intersect the triangle, no subdivision is made. (b) The end of a fault trace intersects the triangle, and the triangle is divided into 4 smaller triangles. (c) If a fault trace crosses the triangle, 5 sub-triangles are constructed. (d) The triangle contains an intersection of fault traces, and is divided into 6 smaller triangles.

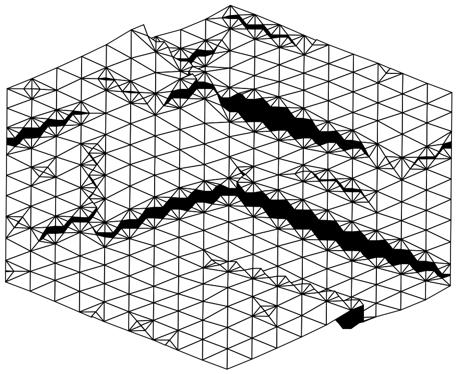

Figure 5: Perspective plot of the topography of the horizon H, constructed by triangulation of the pixels in an image $(\boldsymbol{E}, \boldsymbol{V}, \boldsymbol{P})$. The fault planes, which are all vertical, are colored dark.

3.2 Prior model

The prior model of a faulted horizon should contain general geological knowledge about faults and fault patterns. The prior model of the edges $\boldsymbol{E}$ should thus contain information on typical fault patterns in a horizon, the prior model of the vertices $\boldsymbol{V}$ should reflect characteristics of fault offsets, and the prior model of the pixels $\boldsymbol{P}$ should produce a satisfactory topography of the faulted horizon. Combining the prior distributions of the edges, vertices and pixels, a prior model of the faulted horizon H is obtained. The pdf $f(h)$ of H can be expressed as follows:

$$f(h) = f(\boldsymbol{e}, \boldsymbol{v}, \boldsymbol{p}) = f(\boldsymbol{p}|\boldsymbol{e}, \boldsymbol{v}) f(\boldsymbol{v}|\boldsymbol{e}) f(\boldsymbol{e}). \tag{2}$$

3.2.1 Fault traces

The edges $\boldsymbol{E}$ form an image of fault traces on a horizon, and the prior model of fault traces is based on the work by Tjelmeland and Besag (1998). They consider Markov random fields containing higher order interactions, where a Markov random field is defined on the pixels in the image. In this work a corresponding model is used for the edges. The aim is to include higher order interactions between edges in the image, and to control, to some extent, the pattern of fault traces. The image is represented by a hexagonal grid, as described in Section 3.1. Typical angles of intersection between two fault traces are angles of approximately 60°, which are easily modeled in the hexagonal grid, but angles of around 90° are also common and can be modeled using this grid. Edge effects are accounted for by using circular boundary conditions.

A neighborhood system must be chosen to define the Markov random field used to model

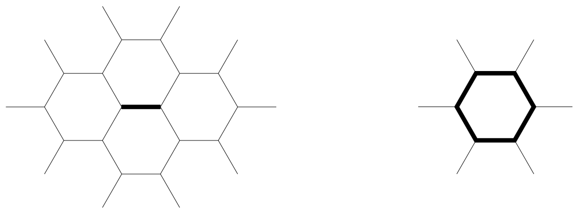

(a) (b)

Figure 6: (a) The neighborhood of the edge in the center, drawn with a thick line, is composed of the edges drawn with thin lines. (b) The maximum clique of the neighborhood in (a). The edges drawn with thick lines form the inner edges, and the edges drawn with thin lines form the outer edges.

the fault traces. The neighborhood illustrated in Figure 6a is used, and the corresponding maximum clique is shown in Figure 6b. The maximum clique consists of the largest set of edges where all pairs of edges are neighbors. The edges contained in the maximum clique are classified as inner and outer edges, where inner edges are drawn with thick lines in Figure 6b, and outer edges with thin lines.

According to the Hammersley-Clifford theorem, see for example Winkler (1995), the distribution of any Markov random field $\boldsymbol{E}$ can be expressed as a Gibbs distribution, see Geman and Geman (1984). The pdf of the Gibbs distribution is given as

$$f(\boldsymbol{e}) = \text{const} \times \exp\{-\sum_{c\in\mathcal{C}} \omega_c(\boldsymbol{e}_c)\}, \tag{3}$$

where $\mathcal{C}$ is the set of all cliques and $\omega_c(\boldsymbol{e}_c)$ is the potential function of the edges $\boldsymbol{e}_c$ contained in the clique c. The sum $\sum_{c\in\mathcal{C}} \omega_c(\boldsymbol{e}_c)$ is called the energy function. Using the neighborhood shown in Figure 6a, possible cliques are the maximum clique shown in Figure 6b and all subsets of the maximum clique. Only the maximum cliques are assigned non-zero potentials in this work. Thus the pdf of the edges $\boldsymbol{E}$ can be expressed as

$$f(\boldsymbol{e}) = \text{const} \times \exp\{-\sum_{c\in\mathcal{C}^m} \omega_c(\boldsymbol{e}_c)\}, \tag{4}$$

where $\mathcal{C}^m \subset \mathcal{C}$ is the set of all maximum cliques. The maximum clique $\boldsymbol{e}_c$ contains 12 edges, where each edge takes a value in the set $\Omega_e = \{0, 1\}$. Thus there are $2^{12} = 4096$ different clique configurations, with a corresponding number of function values $\omega_c(\boldsymbol{e}_c)$. In order to reduce the number of potentials that needs to be specified, the clique configurations are classified into a limited number of classes and all members of a class are assigned equal potentials. A possible classification is shown in Figure 7. Rotations and reflections of the configurations belong to the same class, and are omitted in the figure. The clique configurations in the figure are classified as background, point, end, short-line, line, two-lines, angle, single-cross, double-cross or edge-background. The latter is the class of configurations where all inner edges have value 0, but at least one of the outer edges has a value of 1. All configurations not shown in Figure 7, or not being a rotation or reflection of a configuration in the figure, are classified as other.

The pdf in Expression (4) is defined by specifying potentials $\omega_c(\boldsymbol{e}_c) = \gamma_i$ for the 11 classes of clique configurations. The potentials are given in Table 1. Since any constant can be added or subtracted in the exponent in Expression (4) without changing the prior pdf $f(\boldsymbol{e})$, the critical choice is not the actual potential values, but the differences between the potentials. Thus one class can be assigned a zero potential, and all other potentials are defined relative to this class. The class of edge-background is chosen as a zero potential reference class.

The classification of cliques shown in Figure 7, with the potentials given in Table 1, defines an isotropic distribution of the orientation of fault traces. The configuration classes can be subdivided to produce anisotropic distributions of fault orientation, assigning different potentials to fault traces depending on the direction of the trace. An example of a subdividing of the configuration class line is shown in Figure 8. Directions 1, 3 and 5 are rotations and reflections of the configuration in Figure 7g, while directions 2, 4 and 6 are reflection and rotations of the configuration in Figure 7h.

Subdividing of the configuration classes end, short-line and two-lines can also be applied, based on reflections and rotations of the configurations in Figures 7c-d, 7e-f and 7i-j respectively. The configuration classes angle, single-cross and double-cross contain two or more fault traces of different orientations, and subdividing according to directions is not applied to these classes. Furthermore, neither the configuration classes point, other nor edge-background are subdivided. The total number of potentials are listed in Table 2. The potentials of the subdivided classes are donated $\gamma_{i,j}$, $j = 1, \ldots, 6$, where j gives the direction of the fault trace.

Configuration name	*Configuration* $\boldsymbol{e}_c$	$\omega_c(\boldsymbol{e}_c)$
Background	Fig. 7a	γ_1
Point	Fig. 7b	γ_2
End	Fig. 7c, d	γ_3
Short-line	Fig. 7e, f	γ_4
Line	Fig. 7g, h	γ_5
Two-lines	Fig. 7i, j	γ_6
Angle	Fig. 7k	γ_7
Single-cross	Fig. 7l	γ_8
Double-cross	Fig. 7m	γ_9
Other	Not illustrated	γ_{10}
Edge-background	Fig. 7n	0.0

Table 1: Potentials $\omega_c(\boldsymbol{e}_c) = \gamma_i$ for the configuration classes shown in Figure 7.

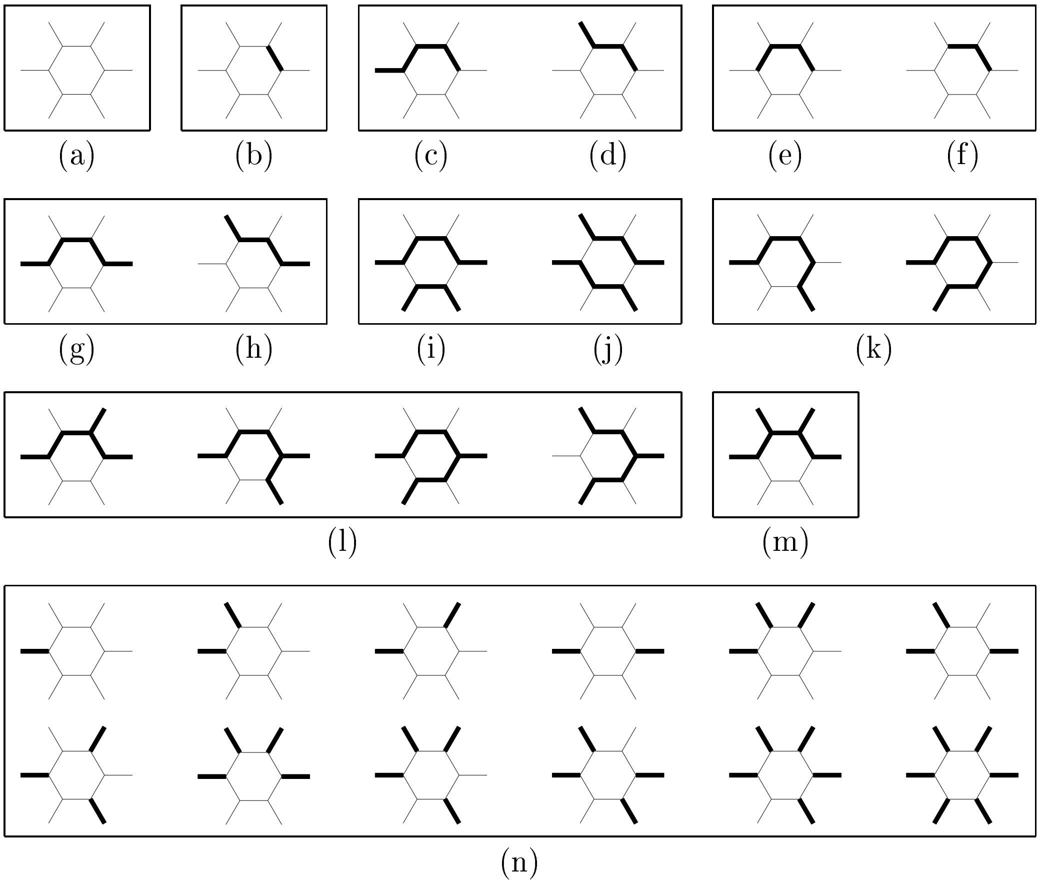

Figure 7: Classes of clique configurations, up to rotation and reflection. Thick solid edges have value $E = 1$, others have value $E = 0$. The clique configurations are classified as (a) background, (b) point, (c)–(d) end, (e)–(f) short-line, (g)–(h) line, (i)–(j) two-lines, (k) angle, (l) single-cross, (m) double-cross and (n) edge-background.

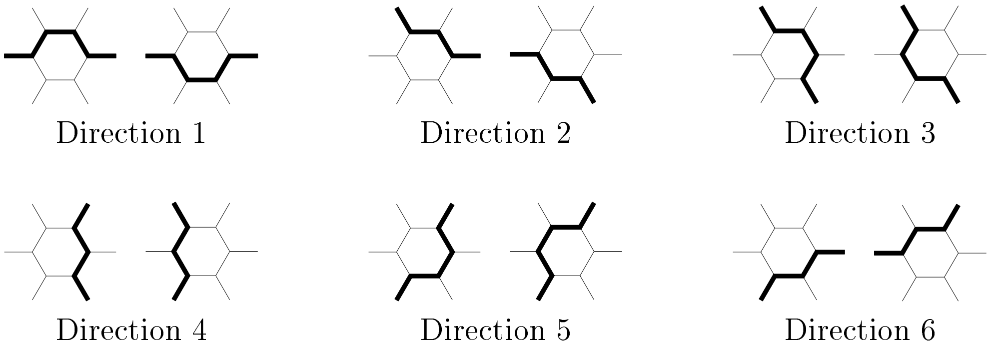

Figure 8: Subdividing of the configuration class line into 6 classes of different orientations.

Configuration name	*Configuration* $\boldsymbol{e}_c$	$\omega_c(\boldsymbol{e}_c)$
Background	Fig. 7a	γ_1
Point	Fig. 7b	γ_2
End	Fig. 7c	$\gamma_{3,1}$, $\gamma_{3,3}$, $\gamma_{3,5}$
	Fig. 7d	$\gamma_{3,2}$, $\gamma_{3,4}$, $\gamma_{3,6}$
Short-line	Fig. 7e	$\gamma_{4,1}$, $\gamma_{4,3}$, $\gamma_{4,5}$
	Fig. 7f	$\gamma_{4,2}$, $\gamma_{4,4}$, $\gamma_{4,6}$
Line	Fig. 7g	$\gamma_{5,1}$, $\gamma_{5,3}$, $\gamma_{5,5}$
	Fig. 7h	$\gamma_{5,2}$, $\gamma_{5,4}$, $\gamma_{5,6}$
Two-lines	Fig. 7i	$\gamma_{6,1}$, $\gamma_{6,3}$, $\gamma_{6,5}$
	Fig. 7j	$\gamma_{6,2}$, $\gamma_{6,4}$, $\gamma_{6,6}$
Angle	Fig. 7k	γ_7
Single-cross	Fig. 7l	γ_8
Double-cross	Fig. 7m	γ_9
Other	Not illustrated	γ_{10}
Edge-background	Fig. 7n	0.0

Table 2: Potentials $\omega_c(\boldsymbol{e}_c)$ when some classes are subdivided to define potentials depending on the orientation of the fault traces. The subscript j of $\gamma_{i,j}$ indicates the direction of the fault trace.

Figures 9 and 10 show independently generated realizations from $f(\boldsymbol{e})$, using the different potentials listed in Table 3. Simulation from the distribution $f(\boldsymbol{e})$ is described in Appendix A, Algorithm 2. Several simulations are run using different potential values, to study the variations in the prior distribution. The number of concentric bands of pixels are 9, resulting in 217 pixels, 702 edges and 486 vertices. Examples 1–4, Figure 9, use isotropic prior distributions of $\boldsymbol{E}$. In examples 5–8, Figure 10, fault traces with orientation in direction NW-SE are favored, which is direction 2 in Figure 8.

In example 1 angles and single-crosses are assigned low potentials, creating fault patterns with a number of bending and intersecting faults. In examples 2–4 the potentials of angles and single-crosses are increased, resulting in fault patterns of isolated, straight fault traces. The pdf used in example 3 has a lower potential for points and short-lines than in example 2, and the fault traces tend to be shorter. In example 4 the potential of points and short-lines is decreased even further. The result is a fault pattern containing a relatively large number of short fault traces.

The realizations in examples 5–8 are generated from anisotropic prior distributions. In examples 6 and 7 the fault patterns are dominated by a number of long fault traces in direction NW-SE. This characteristic is hardly detectable in example 5 where the potentials of direction NW-SE are slightly lower than potentials of the other directions, but angles and single-crosses are assigned low potentials. Direction NW-SE dominates in the realizations of example 8, as it does in examples 6 and 7. However, due to a higher potential for lines,

(a)

Example	Potentials		
No.	γ_1	γ_9	γ_{10}
1–8	-0.1	1.1	3.4

(b)

Example	Potentials						
No.	γ_2	γ_3	γ_4	γ_5	γ_6	γ_7	γ_8
1	1.6	-0.1	1.4	-0.2	1.025	0.0	0.1
2	1.8	-0.1	1.6	-0.2	1.025	0.2	0.9
3	1.6	-0.1	1.4	-0.2	1.025	0.5	0.9
4	1.2	-0.1	1.0	-0.2	1.025	0.5	0.9

(c)

Example	Potentials										
No.	γ_2	$\gamma_{3,2}$	$\gamma_{3,j}$	$\gamma_{4,2}$	$\gamma_{4,j}$	$\gamma_{5,2}$	$\gamma_{5,j}$	$\gamma_{6,2}$	$\gamma_{6,j}$	γ_7	γ_8
5	1.6	-0.2	-0.1	1.3	1.4	-0.25	-0.2	0.925	1.025	0.0	0.1
6	1.6	-0.2	-0.1	1.3	1.4	-0.275	-0.2	0.925	1.025	0.0	0.1
7	1.6	-0.2	-0.1	1.3	1.4	-0.3	-0.2	0.925	1.025	0.0	0.1
8	1.6	-0.2	-0.1	1.3	1.4	-0.2	-0.1	0.925	1.025	0.5	0.9

Table 3: Potentials used in the prior pdf $f(\boldsymbol{e})$. The potentials in (a) are kept constant in all examples. The potentials in (b) give an isotropic prior distribution while the potentials in (c) give an anisotropic prior pdf which favors fault orientations in direction 2, see Figure 8. In the potentials $\gamma_{i,j}$, $i = 3, \ldots, 6$, j takes the values $j = 1, 3, \ldots, 6$.

angles and single-crosses in example 8, the faults are shorter and few intersections are observed.

3.2.2 Fault offsets

The vertices $\boldsymbol{V}$ represent the offsets along fault traces, where the offset tends to vary along a trace. The maximum offset depends on the horizontal extent, or length, of the fault trace, and is typically located near the center point of the trace. Faults with long trace lengths tend to have a larger maximum offset than faults with short trace lengths. A number of geological studies suggest a relationship $D \propto L^{\alpha}$ between maximum displacement D and length L, see for example Walsh and Watterson (1987, 1988), Gauthier and Lake (1993), Dawers et al. (1993).

Fault traces are represented as connected edges of value $E = 1$. A fault trace can have an isolated fault tip, where one end of an edge of value $E = 1$ is only connected to edges of value $E = 0$, as in the clique configurations in Figure 7c-d. Alternatively, the fault trace can terminate in another fault trace, producing a single-cross as in the configurations in Figure 7l, or a double-cross as shown in Figure 7m. The number of faults and their traces

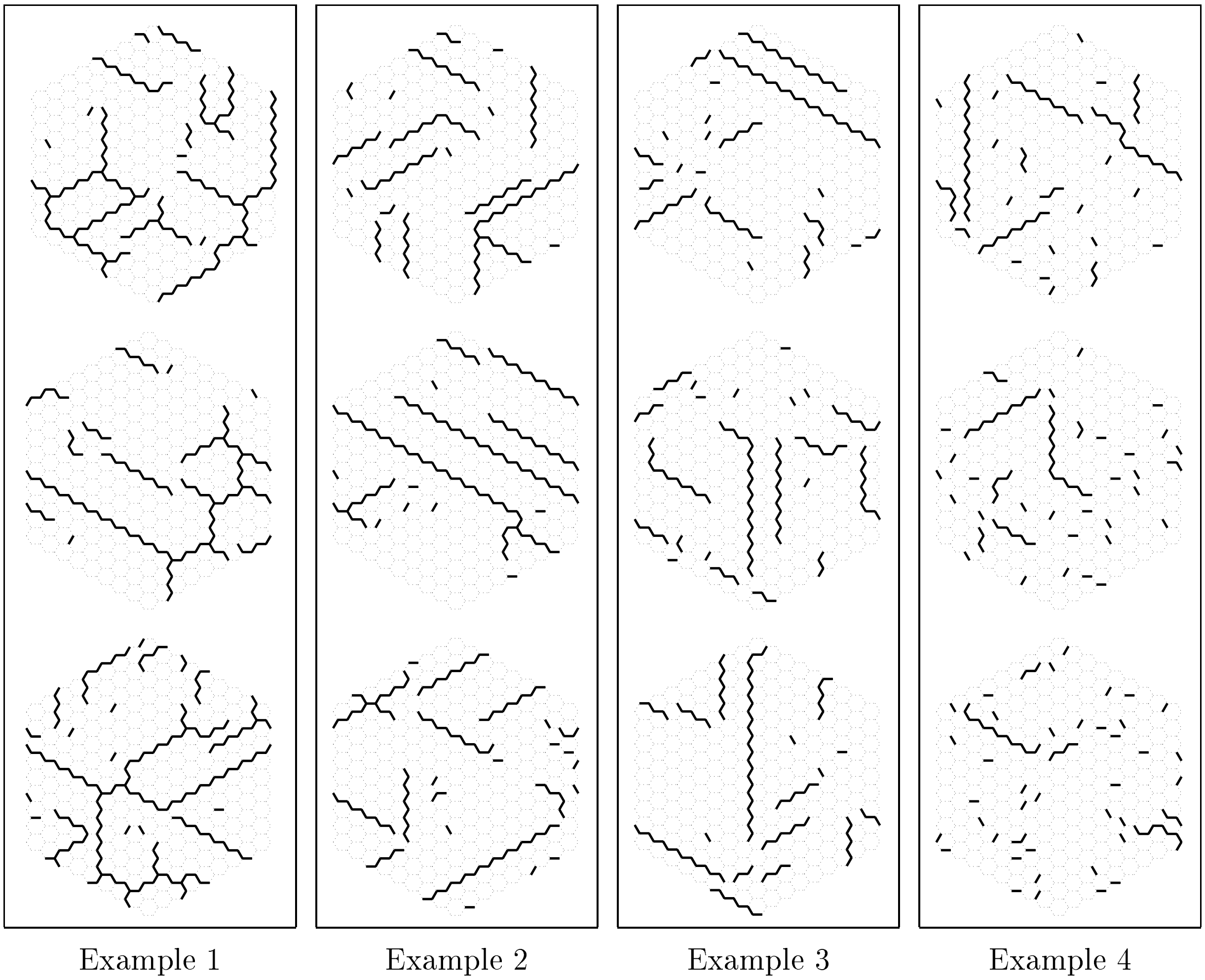

Figure 9: Realizations of $\boldsymbol{E}$ from $f(\boldsymbol{e})$, using different potentials with isotropic distribution of orientation. The potentials are given in Table 3.

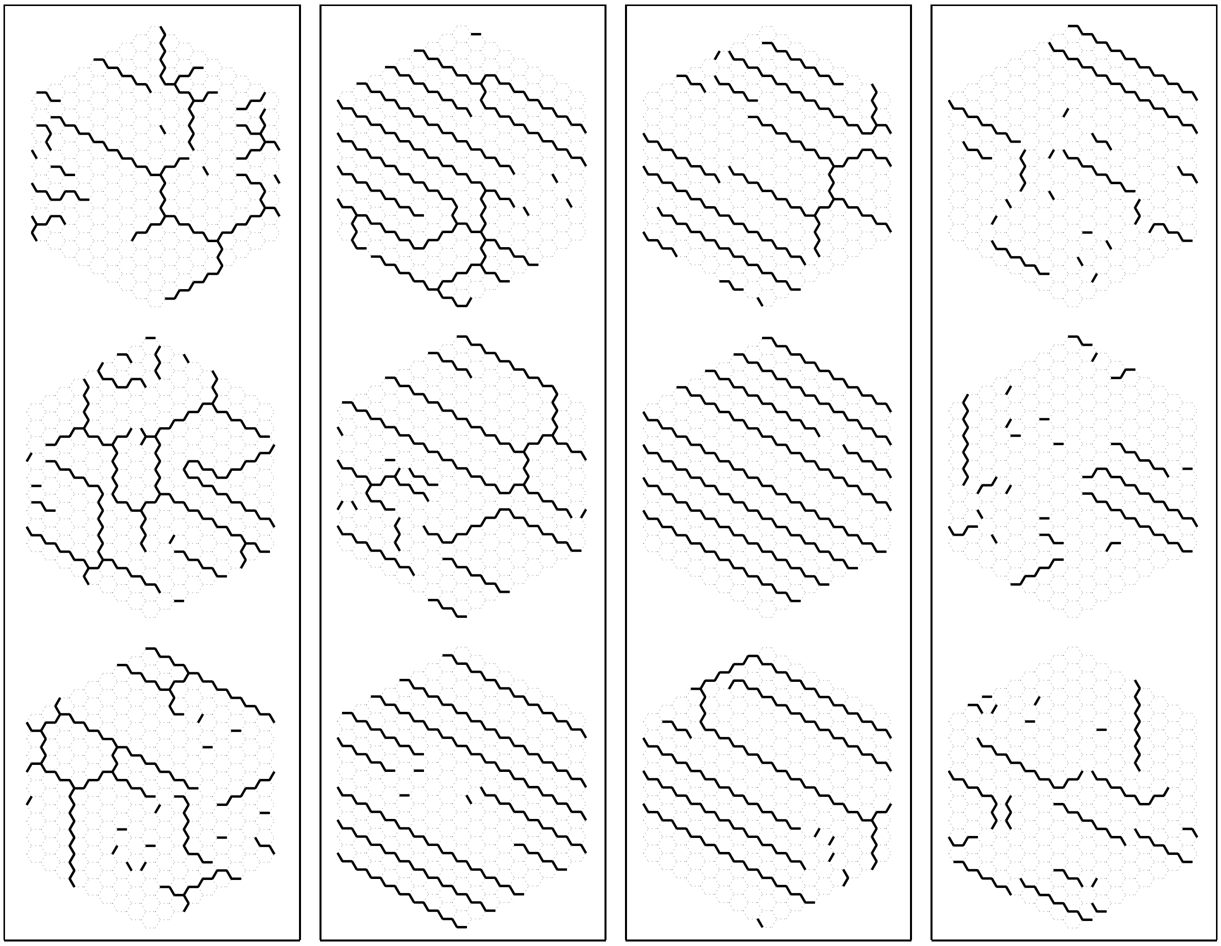

Example 5 Example 6 Example 7 Example 8

Figure 10: Realizations of $\boldsymbol{E}$ from $f(\boldsymbol{e})$, using different potentials with anisotropic distribution of orientation. Direction NW-SE is favored. The potentials are given in Table 3.

are determined by the realization of the edges. The circular boundary conditions used in the prior model of $\boldsymbol{E}$ are adopted.

Let $b \subset \mathcal{V}$ be an index set consisting of all vertices along a fault trace, and let $\mathcal{B}_e = \{b_1, b_2, \ldots, b_n\}$ be the set of all fault traces produced by the edge values $\boldsymbol{E} = \boldsymbol{e}$. Each vertex is defined as belonging to a maximum of one fault trace, thus $b_j \cap b_k = \emptyset$ for any $b_j, b_k \in \mathcal{B}_e$. At intersection points of two traces it is not uniquely defined which two edges belong to the same trace, while the third edge is part of the intersecting trace. Thus for each realization $\boldsymbol{e}$ of edges there is a number, $n_b(\boldsymbol{e})$, of possible ways of defining the set $\mathcal{B}_e$. All these partitionings are assigned equal probability $n_b(\boldsymbol{e})^{-1}$. The index set of all vertices not included in any fault trace is denoted $b_0 = \mathcal{V} \setminus \{\cup_{b_j \in \mathcal{B}_e} b_j\}$, where for any vertex V_i, $i \in b_0$, the common value of all edges connected to the vertex is $E = 0$.

Consider a fault trace $b \in \mathcal{B}_e$ composed of n connected edges of value $E = 1$. The fault trace is classified according to the number of isolated fault tips, $i \in \{0, 1, 2\}$, and is assigned a standardized offset profile $g_i(x, n)$, $x \in [0, 1]$. The offset profile has a maximum at the center point of the fault trace, descending to zero at isolated fault tips. The offset profiles are shown in Figure 11 and are defined as

$$\begin{aligned} g_0(x,n) &= \mu(n) \\ g_1(x,n) &= \begin{cases} 4\mu(n)x(1-x), & x \leq 0.5 \\ \mu(n), & x > 0.5 \end{cases} \\ g_2(x,n) &= 4\mu(n)x(1-x), \end{aligned} \tag{5}$$

where the function $\mu(n)$ is used to model the relationship between the maximum offset and the length n of the fault trace, and is chosen as $\mu(n) = \mu_v n$ where μ_v is a constant. A discrete representation of the offset profile $g_i(x, n)$ is given by the vector $\boldsymbol{g}_{i,n}$, with one component for each vertex along b. The offset values of vertices along the trace are given as $\boldsymbol{V}_b = D_b \boldsymbol{g}_{i,n}$, where the stochastic variable D_b is the offset direction of fault b, with two possible values $D_b \in \{-1, 1\}$. The pdf of the vertex values $\boldsymbol{V}_b$ conditioned on the offset direction D_b is given by $f(\boldsymbol{v}_b|d_b) = \delta(\boldsymbol{v}_b - d_b\boldsymbol{g}_{i,n})$, where $\delta(t)$ is the Dirac delta function. The prior distribution of D_b is chosen as $f(1) = \theta$, $f(-1) = 1 - \theta$, where $0 \leq \theta \leq 1$, resulting in the following pdf of $\boldsymbol{V}_b$:

$$f(\boldsymbol{v}_b) = \sum_{d_b \in \{-1,1\}} f(\boldsymbol{v}_b|d_b) f(d_b) \;=\; \theta\delta(\boldsymbol{v}_b - \boldsymbol{g}_{i,n}) + (1-\theta)\delta(\boldsymbol{v}_b + \boldsymbol{g}_{i,n}). \tag{6}$$

When the offset direction D_b is known, the vertex values $\boldsymbol{V}_b$ are deterministically given. Thus the distribution of the offset along the fault trace b is uniquely defined through the dip parameter θ, the length n of the trace and the size parameter μ_v.

The vertices in b_0 represent points not included in any fault traces. These points have zero offset, implying vertex values of $V_i = 0$, $i \in b_0$. The vertices in b_0 are denoted $\boldsymbol{V}_{b_0} = \{V_i; i \in b_0\}$, and have pdf

$$f(\boldsymbol{v}_{b_0}) = \delta(\boldsymbol{v}_{b_0}). \tag{7}$$

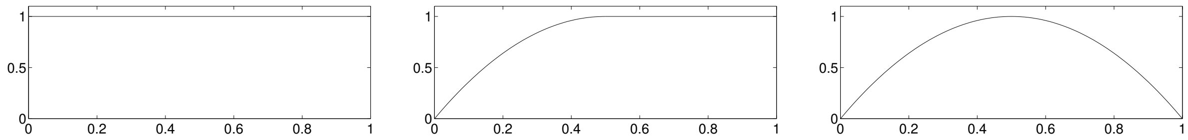

$g_0(x,n)$ $g_1(x,n)$ $g_2(x,n)$

Figure 11: Functions $g_i(x,n)$ representing the standardized offset profiles along a fault trace of i isolated fault tips.

The pdf of all vertices $\boldsymbol{V}$, conditioned on the edges $\boldsymbol{E}$, is obtained by combining the pdfs (6) and (7):

$$f(\boldsymbol{v}|\boldsymbol{e}) = n_b(\boldsymbol{e})^{-1} f(\boldsymbol{v}_{b_0}) \prod_{b\in\mathcal{B}_e} f(\boldsymbol{v}_b), \tag{8}$$

where vertices $\boldsymbol{V}_b$ and $\boldsymbol{V}_{b'}$ are assumed to be independent for any two fault traces $b, b' \in \mathcal{B}_e$. The number of terms in the product depends on the dimension $|\mathcal{B}_e|$ of the set $\mathcal{B}_e$, which is determined by the edge values $\boldsymbol{e}$. The non-zero values of the pdf can be expressed as

$$f(\boldsymbol{v}|\boldsymbol{e}) = n_b(\boldsymbol{e})^{-1}\theta^k(1-\theta)^{|\mathcal{B}_e|-k}, \qquad 0 \le k \le |\mathcal{B}_e|, \tag{9}$$

where k is the number of faults $b \in \mathcal{B}_e$ offset in direction $D_b = 1$.

3.2.3 Topography of faulted surface

The pixels $\boldsymbol{P}$ represent the topography of the faulted horizon. The pattern of fault traces on the horizon and the offsets along the traces are represented by the edges $\boldsymbol{E}$ and vertices $\boldsymbol{V}$ respectively. The pixel values $\boldsymbol{P}$ should produce an image of a surface, reproducing the discontinuities and offsets along the fault traces. Note that absolute depth is not defined, but the pixel values give relative altitudes of the topography of the faulted surface. Edge effects are accounted for by using free boundary conditions.

A multivariate Gaussian distribution is used as a prior model for pixel values. The mean value μ should depend on the edge values $\boldsymbol{E} = \boldsymbol{e}$ and vertex values $\boldsymbol{V} = \boldsymbol{v}$, thus $\mu = \mu(\boldsymbol{e}, \boldsymbol{v})$, while the covariance matrix Σ_p is defined independently of $\boldsymbol{e}$ and $\boldsymbol{v}$. The prior pdf of $\boldsymbol{P}$ is then given as the pdf $\phi(\cdot)$ of the multivariate Gaussian distribution:

$$\begin{aligned} f(\boldsymbol{p}|\boldsymbol{e},\boldsymbol{v}) &= \phi(\boldsymbol{p}; \mu(\boldsymbol{e},\boldsymbol{v}), \Sigma_p) \\ &= (2\pi)^{-n_p/2}|\Sigma_p|^{-n_p/2} \exp\{-(\boldsymbol{p}-\mu(\boldsymbol{e},\boldsymbol{v}))'\Sigma_p^{-1}(\boldsymbol{p}-\mu(\boldsymbol{e},\boldsymbol{v}))/2\}. \end{aligned} \tag{10}$$

The mean values $\mu(\boldsymbol{e},\boldsymbol{v})$ should reflect the discontinuities along fault traces, with the correct offset values across the discontinuities. Consider two adjacent pixels P_i and P_j, where E_{ij} is the edge between the pixels and V_{ij1} and V_{ij2} the vertices at the ends of the edge, see Figure 12. Let $\bar{V}_{ij}$ be the average of the two vertex values. For a given realization $(\boldsymbol{E}, \boldsymbol{V}) = (\boldsymbol{e}, \boldsymbol{v})$, denote by $\mu(\boldsymbol{e}, \boldsymbol{v}) = (\mu_1, \mu_2, \ldots, \mu_{n_p})$ the mean values of the pixels. If an edge E_{ij} is not included in any fault trace, $E_{ij} = 0$, the difference between the mean values of P_i and P_j should be $\mu_i - \mu_j = 0$. If there is a fault trace including the edge, $E_{ij} = 1$, the difference should be approximately $\mu_i - \mu_j = \bar{v}_{ij}$. Generally the requirement is thus

$$\mu_j - \mu_i = e_{ij}\bar{v}_{ij} \quad \forall(i \sim j), \tag{11}$$

where $i \sim j$ denotes adjacent pixels. The equation system is in general singular and has no solution. To overcome this problem the offset values of the vertices are not considered to give the final offsets along the fault traces. Instead the surface of mean values $\mu(\boldsymbol{e}, \boldsymbol{v})$ is approximated according to some optimization criterion. The pixel values only give relative heights of the surface, so without loss of generality the mean value of pixel 1 can be assigned a value $\mu_1 = 0$. The remaining mean values $\mu_2, \ldots, \mu_{n_p}$ are found as a least square solution of the linear equation system (11). The equation system can be expressed as a regression problem $\boldsymbol{Y}(\boldsymbol{e}, \boldsymbol{v}) = \boldsymbol{Z}\beta$ where the components of $\boldsymbol{Y}(\boldsymbol{e}, \boldsymbol{v})$ are given as $e_{ij}\bar{v}_{ij}$, and $\beta = (\mu_2, \mu_3, \ldots, \mu_{n_p})$. The design matrix $\boldsymbol{Z}$ is independent of $\boldsymbol{e}$ and $\boldsymbol{v}$, and has component values $Z_{ij} \in \{-1, 0, 1\}$. The least square fit $\hat{\beta}$ is given by $\hat{\beta} = (\boldsymbol{Z}'\boldsymbol{Z})^{-1}\boldsymbol{Z}'\boldsymbol{Y}(\boldsymbol{e}, \boldsymbol{v})$, and this fit, together with $\mu_1 = 0$, is used as mean values of the pixels $\boldsymbol{P}$. Thus

$$\mu(\boldsymbol{e}, \boldsymbol{v}) = (0, (\boldsymbol{Z}'\boldsymbol{Z})^{-1}\boldsymbol{Z}'\boldsymbol{Y}(\boldsymbol{e}, \boldsymbol{v})). \tag{12}$$

The entries of the covariance matrix Σ_p is given as

$$\mathrm{Cov}(P_i, P_j) = \sigma_p^2 \rho(x_i, x_j), \tag{13}$$

where x_i denotes the position of pixel i. The exponential correlation function is used,

$$\rho(x, x') = \rho(x' - x) = \exp\{-3(|x' - x|/a)^\nu\}, \qquad a > 0,\ 0 < \nu \leq 2, \tag{14}$$

where the parameter a is called the correlation range.

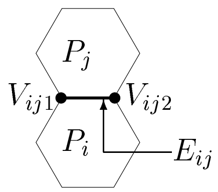

Figure 12: The figure illustrates the notation of adjacent pixels P_i and P_j, the edge E_{ij} between the pixels, and the vertices V_{ij1} and V_{ij2} at the ends of the edge.

3.2.4 Faulted horizon

The image $(\boldsymbol{E}, \boldsymbol{V}, \boldsymbol{P})$ gives a discrete parameterization of the topography of a faulted horizon. A continuous representation H is created by triangulation between the pixel centers, as described in Section 3.1. The topographic surface H is a deterministic function of the image $(\boldsymbol{E}, \boldsymbol{V}, \boldsymbol{P})$, and the pdf of H is given in Expression (2). Inserting Expressions (4), (8) and (10), the following expression of the pdf of H is obtained:

$$
\begin{aligned}
f(h) &= \text{const} \times \phi(\boldsymbol{p}; \mu(\boldsymbol{e}, \boldsymbol{v}), \Sigma_p) \cdot n_b(\boldsymbol{e})^{-1} f(\boldsymbol{v}_{b_0}) \prod_{b \in \mathcal{B}_e} f(\boldsymbol{v}_b) \cdot \exp\{-\sum_{c \in \mathcal{C}^m} \omega_c(\boldsymbol{e}_c)\} \\
&= \text{const} \times \exp\{-(\boldsymbol{p} - \mu(\boldsymbol{e}, \boldsymbol{v}))' \Sigma_p^{-1} (\boldsymbol{p} - \mu(\boldsymbol{e}, \boldsymbol{v}))/2 - \sum_{c \in \mathcal{C}^m} \omega_c(\boldsymbol{e}_c)\} \qquad (15) \\
&\qquad \times n_b(\boldsymbol{e})^{-1} \theta^k (1-\theta)^{|\mathcal{B}_e| - k},
\end{aligned}
$$

where k is the number of faults $b \in \mathcal{B}_e$ offset in direction $D_b = 1$. The number $n_b(\boldsymbol{e})^{-1}$, the dimension $|\mathcal{B}_e|$ of the set $\mathcal{B}_e$, the sets b contained in $\mathcal{B}_e$ and the set b_0 depend on the edge values $\boldsymbol{E}$. Thus the number of terms in the product $\prod_{b \in \mathcal{B}_e} f(\boldsymbol{v}_b)$ will vary, and also the dimensions of the variables $\boldsymbol{V}_b$.

Figure 13 shows a realization of h from the prior pdf $f(h)$. The sampling procedure used to generate this realizations is described in Section 6. The figure shows edges $\boldsymbol{e}$, Figure 13a, vertices $\boldsymbol{v}$, Figure 13b, and pixels $\boldsymbol{p}$, Figure 13c. Figure 13d gives a perspective plot of the continuous surface $h = h(\boldsymbol{e}, \boldsymbol{v}, \boldsymbol{p})$, and the surface is represented as a gray scale image in Figure 13f. Figure 13e shows the final offsets, being the magnitudes of the discontinuities along fault traces in the surface. The figure should be compared with Figure 13b. Away from fault intersections the two figures appear to be quite similar, with only minor differences. Close to fault trace intersections the two figures differ to some extent, indicating that the mean values $\mathrm{E}[\boldsymbol{P}|\boldsymbol{E}, \boldsymbol{V}] = \mu(\boldsymbol{e}, \boldsymbol{v})$, Expression (12), are not able to match the vertex values exactly in these regions.

4 Likelihood Model of Reservoir Specific Observations

Faults alter the geometric structure of a reservoir, and thus influence on the structure of reservoir characteristics. Available observations of the characteristics of subsurface reservoirs are discussed in Section 4.1. The relationship between the observations and the fault pattern is defined through the likelihood function, and is described in Section 4.2.

4.1 Observations

Available observations from a subsurface reservoir consist of three dimensional seismic data and well observations. Observations from seismic surveys give a good spatial covering of the reservoir. However, only faults with displacement above 15–20 meters can be resolved

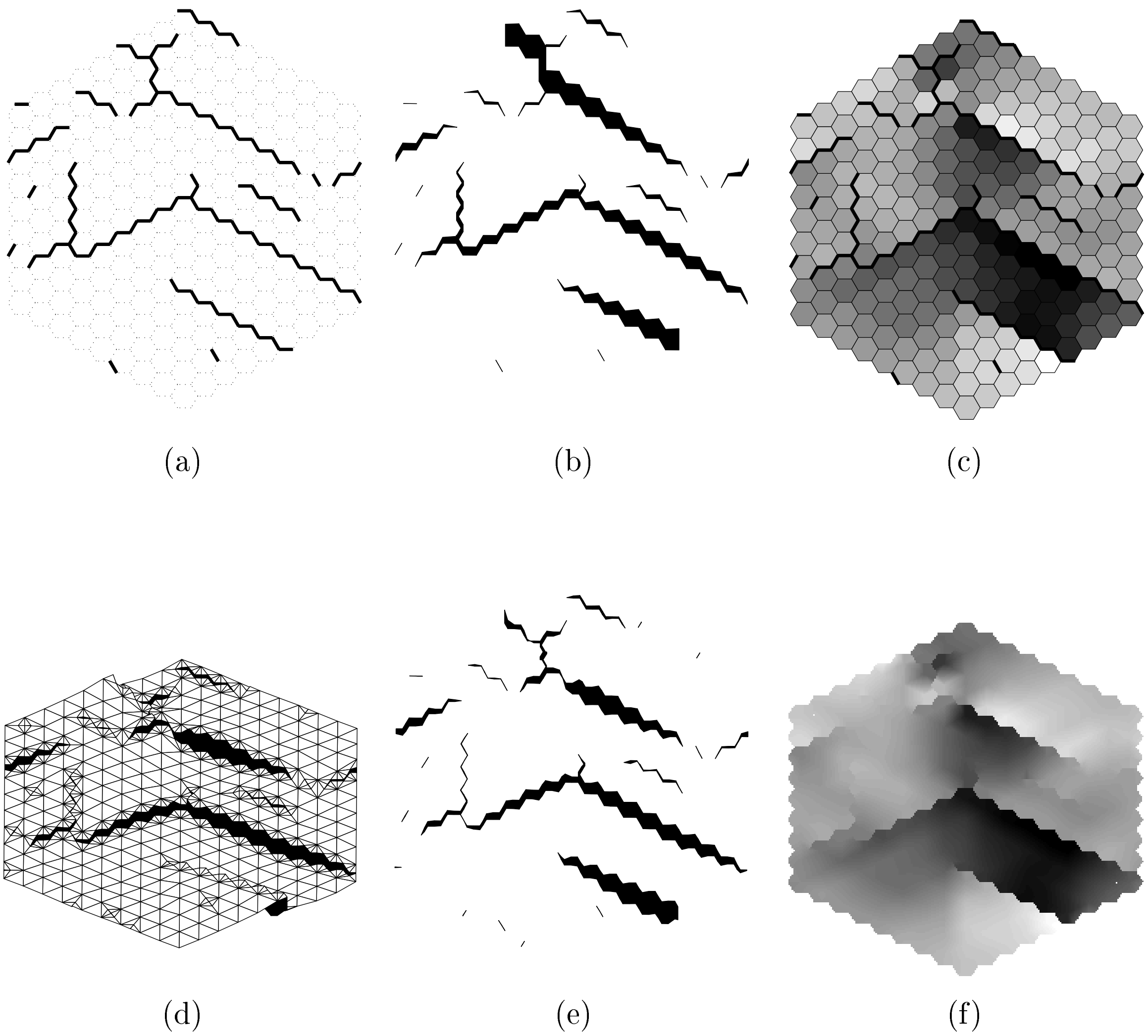

Figure 13: Realization h from the prior pdf (15). (a) Edges $\boldsymbol{e}$ from $f(\boldsymbol{e})$, (b) vertices $\boldsymbol{v}$ from $f(\boldsymbol{v}|\boldsymbol{e})$ and (c) pixels $\boldsymbol{p}$ from $f(\boldsymbol{p}|\boldsymbol{e},\boldsymbol{v})$. (d) Perspective plot of the faulted horizon h, obtained by triangulation of the image $(\boldsymbol{e},\boldsymbol{v},\boldsymbol{p})$. (e) Fault planes from figure (d), showing the true offsets of the faults. (f) Horizon h represented as a gray-scale image.

from seismic data, and the observations contain measurement errors. See for example Sheriff and Geldart (1995) for an introduction to seismic theory. Fine scale observations of reservoir characteristics can be obtained from well logs. Such observations are however few and sparse. Under the assumption of vertical faults, macroscopic faults are not observable in wells. Seismic travel time is used as the vertical scale, while the conversion from time to depth is beyond the scope of this work.

4.1.1 Seismic data

When a seismic wave travels downwards and hits an acoustic impedance discontinuity, a part of the wave is reflected, and the reflected signal is registered at the surface. For P-waves, also denoted longitudinal or compressional waves, the acoustic impedance Z is given as the product of the P-wave velocity α and the density ρ of the medium, $Z = \alpha\rho$. Discontinuities in acoustic impedance are called reflectors, and the most common reflectors are unconformities and significant changes in lithology, see Sheriff and Geldart (1995). Consider a reflector where the P-wave velocity, density and acoustic impedance on one side is α_1, ρ_1 and $Z_1 = \alpha_1\rho_1$ respectively, and on the opposite side α_2, ρ_2 and $Z_2 = \alpha_2\rho_2$. The reflection coefficient at the discontinuity is defined as

$$C = \frac{Z_2 - Z_1}{Z_2 + Z_1}. \tag{16}$$

For a fixed point (x, y) in a horizontal grid of observations, the seismic amplitudes obtained from reflection points along a vertical axis in (x, y) are denoted $S^o(x, y, t)$. The seismic data can be expressed as a convolution of the reflection coefficients $C(x, y, t)$ with a seismic wavelet $w(t) = w(t; \psi_s)$, where ψ_s is a wavelet parameter. The scale of the vertical axis is travel time t, and the superscript o denotes observations throughout this work. A simplification is used, assuming all ray-paths of the seismic wave are vertical, and that all reflectors are horizontal. The seismic data are given by

$$S^o(x, y, t) = w(t) * C(x, y, t) + U(x, y, t) = \int_{-\infty}^{\infty} w(\tau)C(x, y, t - \tau)\, d\tau + U(x, y, t), \tag{17}$$

where $U(x, y, t) \sim N(0, \sigma_s^2)$ is a random noise term including both modeling error and measurement error, see Eide (1999). An approximation to (17) is given by a discrete representation. Assume seismic observations are available for times $t_1, t_2, \ldots, t_n$, and let $S_k^o = S^o(x, y, t_k)$ be the seismic observation at the point (x, y, t_k). The discrete representation of the seismic observation is as follows:

$$S_k^o = \sum_{i=-L}^{L} w_i c_{k-i} \delta t + U_k, \tag{18}$$

where $U_k = U(x, y, t_k)$ is the noise term, $w_i = w(t_i)$ is the seismic wavelet evaluated at time t_i, $c_{k-i} = C(x, y, t_{k-i})$ is the reflection coefficient at time t_{k-i} and $\delta t = t_{i+1} - t_i$ is the time step. Corresponding to Expression (18), an expression of all seismic observations, denoted $\boldsymbol{S}^o$, is given as

$$\boldsymbol{S}^o = A(\psi_s)\boldsymbol{C} + \boldsymbol{U}, \tag{19}$$

where $\boldsymbol{C}$ is a matrix of reflection coefficients, $A(\psi_s)$ is a matrix with entries corresponding to the product $w_i \delta t$ and $\boldsymbol{U}$ a matrix of independent random noise. A commonly used wavelet is the Ricker wavelet, expressed as

$$w(t) = (1 - 2(\pi \nu_M t)^2)\exp(-(\pi \nu_M t)^2), \tag{20}$$

where the wavelet parameter $\psi_s = \nu_M$ is the peak frequency, see Sheriff and Geldart (1995). The Ricker wavelet is symmetric with a maximum at $t = 0$, see Figure 14.

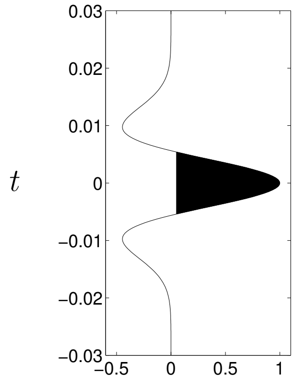

Figure 14: The Ricker wavelet (20) with peak frequency $\nu_M = 40Hz$.

4.1.2 Well observations

From well logs velocity α and density ρ can be derived. The acoustic impedance $Z = \alpha\rho$ can then be calculated, and for vertical wells Expression (16) can be used to obtain reflection coefficients $C(x, y, t)$ in a well located at (x, y). Denote the vector of observed reflection coefficients $\boldsymbol{C}^o$. The observations of reflection coefficients from wells are a subset of the reflection coefficients $\boldsymbol{C}$. Throughout this work well observations are assumed to be exact observations.

4.2 Likelihood model

Two types of observations are discussed in Section 4.1, seismic data and observations of reflection coefficients from well logs. The likelihood model of the seismic data and reflection coefficients is based on the work by Eide (1999). See also Eide et al. (1997a), Eide et al. (1997b). The likelihood function of the reflection coefficients $\boldsymbol{C}$ and $\boldsymbol{C}^o$ is discussed first. The likelihood function of the seismic data $\boldsymbol{S}^o$ and the joint likelihood function of all observations $\boldsymbol{O} = (\boldsymbol{S}^o, \boldsymbol{C}^o)$ are obtained from Expression (17) or (19), based on the likelihood function of the reflection coefficients.

4.2.1 Reflection coefficients

A likelihood function of reflection coefficients in a non-faulted reservoir is first defined. Adjustments are then made to find the likelihood function of the reflection coefficients in the faulted reservoir.

Consider a sedimentary reservoir prior to faulting. Due to the sedimentation process the rock tends to have a layered structure, with a relatively strong lateral homogeneity. Vertically the layered rock is non-homogeneous. Prior to faulting, reflection coefficients of a layered rock can in some cases be modeled as a Gaussian random field, see Todoeschuck et al. (1990) and Eide (1999). Let $\boldsymbol{C}_u$ denote reflection coefficients of a non-faulted reservoir, with a Gaussian distribution

$$\boldsymbol{C}_u \sim N(\mu_{c_u}, \Sigma_{c_u}), \tag{21}$$

where μ_{c_u} is a vector of mean values and Σ_{c_u} is the covariance matrix of $\boldsymbol{C}_u$. The covariance between reflection coefficients in the points (x_i, y_j, t_k) and (x_l, y_m, t_n) is given as

$$\text{Cov}\{C_u(x_i, y_j, t_k), C_u(x_l, y_m, t_n)\} = \sigma^2_{c_u} \rho_{c_u}((x_i, y_j, t_k), (x_l, y_m, t_n)), \tag{22}$$

where $\rho_{c_u}(\cdot)$ is the correlation function of the reflection coefficients and $\sigma^2_{c_u}$ the variance. The lateral homogeneity of the rock is accounted for by defining a strong horizontal correlation in the likelihood model. A correlation function with negative correlation at short vertical ranges is used, suggested by Eide (1999). The horizontal and vertical correlations are assumed to be separable, and are defined based on the exponential correlation function (14). Let $\rho_H(\cdot)$ and $\rho_V(\cdot)$ denote exponential correlation function with range $a = a_H$ and $a = a_V$ respectively. The correlation between $C_u(x_i, y_j, t_k)$ and $C_u(x_l, y_m, t_n)$ can be expressed as

$$\begin{aligned}\rho_{c_u}((x_i, y_j, t_k), (x_l, y_m, t_n)) \;&=\; \rho_H((x_i, y_j), (x_l, y_m)) \times \\ &\{2(1 - \rho_V(\delta t))\}^{-1}\{2\rho_V(t_k, t_n) - \rho_V(t_{k+1}, t_n) - \rho_V(t_k, t_{n+1})\}\end{aligned} \tag{23}$$

where $\rho_H((x_i, y_j), (x_l, y_m))$ is the horizontal correlation and the expression on the last line is the vertical correlation. A regular grid with vertical spacing $t_{i+1} - t_i = \delta t$ is used. A strong horizontal correlation is obtained by assigning a large value to the correlation range a_H. The vertical correlation, corresponding to $(i, j) = (l, m)$ in the correlation function (23), is illustrated in Figure 15.

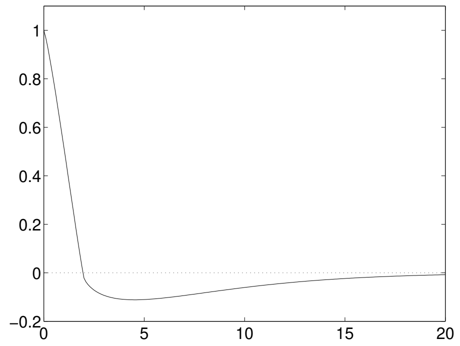

Figure 15: The vertical correlation in the correlation function (23), with parameters $\nu = 1.2$ and $a_V = 15$ in the exponential correlation function $\rho_V(\cdot)$ involved in Expression (23). The scale of the horizontal axis is milliseconds.

After faulting the original structure of the rock is altered. The fault pattern is represented by the horizon $H(x, y)$. Under the basic model assumptions discussed in Section 2, the reflection coefficients originally located in (x, y, t) is displaced to the point $(x, y, t - H(x, y))$, see Figures 16a and 16b. If the faulted horizon $H(x, y)$ is known, the reflection coefficients can be transformed back to their original location, as illustrated in Figure 16c.

Let $C(x, y, t)$ denote the reflection coefficient at a point (x, y, t) in the faulted reservoir. The value of this reflection coefficient is

$$C(x, y, t) = C_u(x, y, t + H(x, y)), \tag{24}$$

obtained by a vertical transformation of the original reflection coefficients C_u. The marginal distributions of the reflection coefficients are unchanged, but due to the spatial rearrangement the mean vector μ_{c_u} and covariance matrix Σ_{c_u} are no longer valid. Consider two points (x, y, t) and (x', y', t') prior to faulting, with reflection coefficients C_u and C'_u. The covariance between the reflection coefficients prior to faulting is given in Expression (22).

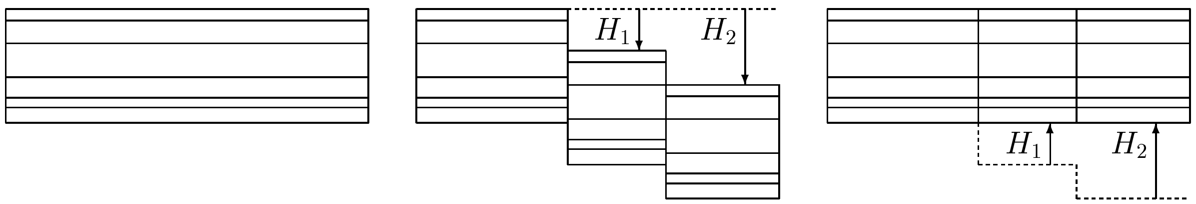

(a) (b) (c)

Figure 16: (a) The structure of the rock before faulting. (b) After faulting the structure is altered. (c) If the faulted horizon H is known, a transformation back to the original structure can be performed.

After faulting the covariance between the two reflection coefficients is unchanged, since the values of the reflection coefficients are not altered by the faulting. However, the positions are changed, and the reflection coefficients considered are now located at $(x, y, t - H(x, y))$ and $(x', y', t' - H(x', y'))$ respectively. The transformations due to faulting can be expressed as a permutation of the elements of the vector $\boldsymbol{C}_u$ of reflection coefficients, and a corresponding rearrangement of the order of the elements in the mean vector μ_{c_u} and covariance matrix Σ_{c_u}. The overall distribution of reflection coefficients in a faulted reservoir is then a Gaussian distribution, expressed as

$$[\boldsymbol{C}|H = h] \sim N(\mu_c(h), \Sigma_c(h)), \tag{25}$$

where $\mu_c(h)$ and $\Sigma_c(h)$ are obtained from μ_{c_u} and Σ_{c_u} by rearranging the positions of the elements according to the transformations dictated by the faulted horizon $H = h$. Reflection coefficients $\boldsymbol{C}^o$ observed in wells are a subset of the reflection coefficients $\boldsymbol{C}$. The observed reflection coefficients follow a Gaussian distribution

$$[\boldsymbol{C}^o|H = h] \sim N(\mu_{c^o}(h), \Sigma_{c^o}(h)), \tag{26}$$

where $\mu_{c^o}(h)$ and $\Sigma_{c^o}(h)$ are subsets of $\mu_c(h)$ and $\Sigma_c(h)$ respectively.

4.2.2 Seismic data

The likelihood function of seismic data $\boldsymbol{S}^o$ is obtained by using the relationship between seismic observations and reflection coefficients given in Expression (17) or (19), and the likelihood model of the reflection coefficients given in Expression (25). The seismic data are linear combinations of the reflection coefficients and a random noise term, both Gaussian random fields, thus the seismic observations are also modeled as a Gaussian random field. The mean and variance functions of the seismic data are found from the mean and variance functions of the reflection coefficients and the random noise term.

Similar to the reflection coefficients, the seismic data can be expressed as a transformation:

$$S^o(x, y, t) = S_u^o(x, y, t + H(x, y)). \tag{27}$$

Using the same notation as in Expression (24), S_u^o denotes the seismic observation that would be obtained if seismic data were gathered prior to faulting of the reservoir. The mean value of $S_u^o(x, y, t)$ is found from Expression (17):

$$\mathrm{E}\{S_u^o(x, y, t)\} = \int_{-\infty}^{\infty} w(\tau)\mu_{c_u}(x, y, t - \tau)\, d\tau. \tag{28}$$

The covariance between seismic observations $S_u^o(x_i, y_j, t_k)$ and $S_u^o(x_l, y_m, t_n)$ is found to be

$$\begin{aligned}\mathrm{Cov}\{S_u^o(x_i, y_j, t_k), S_u^o(x_l, y_m, t_n)\} &= \sigma_s^2 \mathbf{1}[(i, j, k) = (l, m, n)] + \\ \sigma_{c_u}^2 \int_{-\infty}^{\infty}\int_{-\infty}^{\infty} w(\tau_1)w(\tau_2)\rho_{c_u}&((x_i, y_j, t_k - \tau_1), (x_l, y_m, t_n - \tau_2))d\tau_1\, d\tau_2\end{aligned} \tag{29}$$

where $\mathbf{1}[\cdot]$ is the indicator function. The covariance function (22) and the correlation function (23) of the reflection coefficients are used. Using the discrete matrix representation (19), the mean values and covariance matrix of the seismic data $\boldsymbol{S}_u^o$ are found to be

$$\mu_{s_u^o} = \mathrm{E}\{\boldsymbol{S}_u^o\} = A(\psi_s)\mu_{c_u} \qquad \text{and} \qquad \Sigma_{s_u^o} = \mathrm{Var}\{\boldsymbol{S}_u^o\} = A(\psi_s)\Sigma_{c_u}A(\psi_s)' + \sigma_s^2 I, \tag{30}$$

where I is the identity matrix. As for the reflection coefficients, the seismic observations of the faulted reservoir can be modeled as a Gaussian random field with mean vector and covariance matrix depending on the faulted horizon H. The distribution of the seismic data is the Gaussian distribution

$$[\boldsymbol{S}^o|H = h] \sim N(\mu_{s^o}(h), \Sigma_{s^o}(h)) \tag{31}$$

where $\mu_{s^o}(h)$ and $\Sigma_{s^o}(h)$ are obtained by rearranging the elements of $\mu_{s_u^o}$ and $\Sigma_{s_u^o}$ according to the faulted horizon $H = h$.

4.2.3 Joint likelihood model of observations

Reflection coefficients $[\boldsymbol{C}|H]$ are Gaussian distributed, see Expression (25). From Expression (19) it is clear that the joint distribution of $[(\boldsymbol{S}^o, \boldsymbol{C})|H]$ is also Gaussian, and consequently, so is the distribution of the subset $[\boldsymbol{O}|H]$ of observations, where $\boldsymbol{O} = (\boldsymbol{S}^o, \boldsymbol{C}^o)$. By the same arguments as above, the mean vector and covariance matrix of $[\boldsymbol{O}|H]$ can be found by first deriving the corresponding mean and covariance in a non-faulted reservoir, using Expressions (17) or (19), and then rearranging the elements according to the faulted horizon $H = h$. Thus $[\boldsymbol{O}|H = h] \sim N(\mu_o(h), \Sigma_o(h))$, and the joint likelihood function $f(\boldsymbol{o}|h) = f(\boldsymbol{s}^o, \boldsymbol{c}^o|h)$ of the observations $\boldsymbol{O} = (\boldsymbol{S}^o, \boldsymbol{C}^o)$, given H, is the pdf of the Gaussian distribution:

$$f(\boldsymbol{o}|h) = \phi(\boldsymbol{o}; \mu_o(h), \Sigma_o(h)), \tag{32}$$

see Expression (10). The single elements of the covariance matrix $\Sigma_o(h)$ are defined by the covariance function (22) and the matrix $A(\psi_s)$ involved in the convolution (19), while the order of the elements are determined by the faulted horizon H.

5 Posterior Model of Geological Fault Patterns Conditioned to Reservoir Specific Observations

Observations $\boldsymbol{O}$ of the reservoir contain seismic data and observations of reflection coefficients obtained from well logs. The observations carry information about the structure of the reservoir, and how the originally horizontal layers of the reservoir have been altered due to faulting. The aim of this work is to generate realizations of the underlying geological fault pattern, by sampling the faulted horizon H conditioned to the observations. The prior distribution from Section 3 and the likelihood function from Section 4 are combined to form a posterior distribution. Samples from the posterior distribution can be obtained using the methodology presented in Section 6.

The prior pdf $f(h)$ contains general geological knowledge about the fault pattern and the faulted horizon H. The likelihood function $f(\boldsymbol{o}|h)$ gives the likelihood of observing $\boldsymbol{O}$, if the true faulted horizon is H. The posterior distribution

$$f(h|\boldsymbol{o}) = \text{const} \times f(h)f(\boldsymbol{o}|h) \tag{33}$$

combines the general geological knowledge with the reservoir specific observations, and gives the distribution of the faulted horizon H conditioned to the observations $\boldsymbol{O}$. The prior pdf and the likelihood function are given in Expressions (15) and (32) respectively. Inserting the functions into Expression (33), the following posterior pdf is obtained:

$$\begin{aligned} f(h|\boldsymbol{o}) \;\; = \;\; & \text{const} \times \phi(\boldsymbol{p}; \mu(\boldsymbol{e}, \boldsymbol{v}), \Sigma_p) \cdot n_b(\boldsymbol{e})^{-1} f(\boldsymbol{v}_{b_0}) \prod_{b \in \mathcal{B}_e} f(\boldsymbol{v}_b) \cdot \exp\{-\sum_{c \in \mathcal{C}^m} \omega_c(\boldsymbol{e}_c)\} \\ & \times \phi(\boldsymbol{o}; \mu_o(h), \Sigma_o(h)). \end{aligned} \tag{34}$$

The posterior model contains a number of parameters, which are listed in Table 4.

	Prior distribution $f(h) = f(\boldsymbol{p}|\boldsymbol{e}, \boldsymbol{v})f(\boldsymbol{v}|\boldsymbol{e})f(\boldsymbol{e})$*:*
$f(\boldsymbol{e})$:	Potential function $\omega_c(\boldsymbol{e}_c)$: γ_i, $\gamma_{i,j}$, $i = 1, \ldots, 10$, $j = 1, \ldots, 6$
$f(\boldsymbol{v}|\boldsymbol{e})$:	Dip parameter θ
	Size parameter μ_v
$f(\boldsymbol{p}|\boldsymbol{e}, \boldsymbol{v})$:	Variance σ_p^2
	Correlation function $\rho(\cdot)$: ν, a

	Likelihood function $f(\boldsymbol{o}|h) = f(\boldsymbol{s}^o|\boldsymbol{c}^o, h)f(\boldsymbol{c}^o|h)$*:*
$f(\boldsymbol{c}^o|h)$:	Mean μ_c
	Variance σ_c^2
	Correlation function $\rho_c(\cdot)$: ν, a_H, a_V
$f(\boldsymbol{s}^o|\boldsymbol{c}^o, h)$:	Variance σ_s^2
	Ricker wavelet $w(t)$: ν_M
	Time step δt

Table 4: Parameters in the posterior distribution $f(h|\boldsymbol{o})$.

6 Sampling From the Posterior Distribution

Expression (34) gives the posterior pdf of the faulted horizon $H(\boldsymbol{E}, \boldsymbol{V}, \boldsymbol{P})$, conditioned to the observations $\boldsymbol{O}$. Fault patterns and corresponding faulted horizons can be generated by sampling from the posterior distribution. The posterior distribution is high dimensional, and due to the complexity of the distribution no procedure for exact simulation exists. Instead, Markov chain Monte Carlo (McMC) techniques are used, see Besag et al. (1995) for an introduction to McMC methodology and for further references.

A Metropolis-Hastings algorithm is used to generate samples from the posterior distribution $f(h|\boldsymbol{o})$ in (34), see Hastings (1970). A detailed description is given in Algorithm 1, Appendix A. In each step of the algorithm, one of three possible transition types is chosen. Suppose at one step the edge, vertex and pixel values are $\boldsymbol{E} = \boldsymbol{e}$, $\boldsymbol{V} = \boldsymbol{v}$ and $\boldsymbol{P} = \boldsymbol{p}$, and the faulted horizon is $H(\boldsymbol{E}, \boldsymbol{V}, \boldsymbol{P}) = h(\boldsymbol{e}, \boldsymbol{v}, \boldsymbol{p})$. New values $\boldsymbol{e}'$, $\boldsymbol{v}'$ and $\boldsymbol{p}'$ are suggested using one of the transition types. The three alternative transition types have different transition kernels, and are given as follows:

(i) Edge values $\boldsymbol{e}'$, vertex values $\boldsymbol{v}'$ and pixel values $\boldsymbol{p}'$ are generated from the prior distribution, with the transition kernel

$$q(h'|h) = f(\boldsymbol{e}', \boldsymbol{v}', \boldsymbol{p}') = f(\boldsymbol{e}')f(\boldsymbol{v}'|\boldsymbol{e}')f(\boldsymbol{p}'|\boldsymbol{e}', \boldsymbol{v}').$$

(ii) Edge values $\boldsymbol{e}' = \boldsymbol{e}$ are fixed while vertex values $\boldsymbol{v}'$ and pixel values $\boldsymbol{p}'$ are generated from their respective prior distributions. The transition kernel is in this case

$$q(h'|h) = f(\boldsymbol{v}', \boldsymbol{p}'|\boldsymbol{e}) = f(\boldsymbol{v}'|\boldsymbol{e})f(\boldsymbol{p}'|\boldsymbol{e}, \boldsymbol{v}').$$

(iii) Edge values $\boldsymbol{e}' = \boldsymbol{e}$ and vertex values $\boldsymbol{v}' = \boldsymbol{v}$ are fixed while pixel values $\boldsymbol{p}'$ are generated from the prior distribution. In this case the transition kernel is

$$q(h'|h) = f(\boldsymbol{p}'|\boldsymbol{e}, \boldsymbol{v}).$$

In alternative (i) and (ii) the prior density function $f(\boldsymbol{v}|\boldsymbol{e})$ cancels in the acceptance probability, while in alternative (iii) the vertex values $\boldsymbol{V}$ are constant. Thus the dependence of $\mathcal{B}_e$ on $\boldsymbol{E}$ causes no problems in the McMC algorithm, and the number $n_b(\boldsymbol{e})^{-1}$ need not be evaluated. For all suggested transitions, the probability of accepting the proposed horizon $h' = h'(\boldsymbol{e}', \boldsymbol{v}', \boldsymbol{p}')$ is given by

$$\alpha(h'|h) = \min\left\{1,\ \frac{f(\boldsymbol{o}|h')}{f(\boldsymbol{o}|h)}\right\}. \tag{35}$$

A sample from the pdf $f(h)$ is generated in a stepwise procedure, and Figure 13 illustrates the realizations obtained at different steps of the procedure. First, all edge values $\boldsymbol{E}$ are generated from the prior pdf $f(\boldsymbol{e})$. Next, vertex values $\boldsymbol{V}$ are generated from the prior pdf

$f(\boldsymbol{v}|\boldsymbol{e})$ conditioned on the edge values. The pixel values $\boldsymbol{P}$ are then generated from the prior pdf $f(\boldsymbol{p}|\boldsymbol{e},\boldsymbol{v})$ conditioned on both edge and vertex values.

A Metropolis-Hastings algorithm is used to generate realizations from the prior pdf $f(\boldsymbol{e})$, while exact sampling of the offsets and pixels from $f(\boldsymbol{v}|\boldsymbol{e})$ and $f(\boldsymbol{p}|\boldsymbol{e},\boldsymbol{v})$ are easily performed. Algorithms for drawing samples of $\boldsymbol{E}$, $\boldsymbol{V}$ and $\boldsymbol{P}$ from their respective prior distributions are given in Appendix A.

The sample space $\Omega = \Omega_e^{n_e} \times \Omega_v^{n_v} \times \Omega_p^{n_p}$ of H is a high dimensional space, and a large number of iterations must be run in order to span the space adequately. Thus the algorithm is rather time consuming and as n_e, n_v and n_p increase, the number of iterations required increases drastically. In alternative (i) of the transition steps, one further McMC simulation is run within a step of the original McMC algorithm. Thus realizations from the posterior distribution is generated using a double McMC algorithm. However, the McMC algorithm used to sample from the prior pdf $f(\boldsymbol{e})$ is not very time consuming and seems to converge relatively fast, see Section 7.

The simplicity of the likelihood function is an advantage of the described algorithm. All acceptance probabilities are given as a likelihood ratio, where the likelihood function (32) is the pdf of a multivariate Gaussian distribution. Thus the algorithm is capable of handling densely scattered seismic observations, although evaluation of the likelihood function in the case of a large number of observations can be time consuming. Still, the major influence on the time consumption of the algorithm is from the large number of iterations required to span the sample space of H through generation of samples from the prior pdf.

For small datasets the Gaussian likelihood function can be evaluated exactly. As the dimension increases however, the likelihood can in practice not be obtained analytically for general Gaussian fields, and an approximation to the likelihood function must be found. The likelihood function of the observations $\boldsymbol{O}$ can be approximated by a pseudo-likelihood function (Besag, 1974)

$$f(\boldsymbol{o}|h) \approx \prod_i f(\boldsymbol{o}_i|\boldsymbol{o}_{-i},h) \approx \prod_i f(\boldsymbol{o}_i|\boldsymbol{o}_{\partial i},h), \tag{36}$$

where $\boldsymbol{O}_i$ is chosen as a vertical column through the observations and $\boldsymbol{O}_{-i}$ is the set of all other observations. The conditional distributions of $\boldsymbol{O}_i$ are approximated by distributions depending only on observations $\boldsymbol{O}_{\partial i}$ in a neighborhood ∂i of $\boldsymbol{O}_i$. A neighborhood of 5×5 vertical columns is used in the simulations presented below.

7 Sampling From the Prior Model of Fault Traces

The McMC algorithm presented in Section 6 includes sampling from the prior distribution of H, where McMC techniques are also applied to sample from $f(\boldsymbol{e})$. Realizations from

$f(\boldsymbol{e})$ are shown in Figures 9 and 10, and are generated using the McMC algorithm described in Appendix A, Algorithm 2. The convergence of this McMC algorithm is studied in this section.

Figure 17 shows convergence plots for realizations from the prior pdf $f(\boldsymbol{e})$, using the potentials from example 1 in Table 3. The McMC algorithm is run for 20 000 iterations. Each iteration consists of n_e update steps, where at each step an edge is drawn at random, a change of value is suggested, and the new value is accepted with the appropriate probability. The plots in Figure 17 show the relative number of configurations belonging to some of the configuration classes from Table 1, plotted for every 10th iteration. All plots indicate a fast convergence of the algorithm. The Markov chain in Figure 17 has an initial state where each edge value is drawn at random from $\Omega_e = \{0, 1\}$. In Figure 18 some of the plots are compared to Markov chains starting at extreme initial states, one where all edge values are $E = 0$ and one where all are $E = 1$. The first 1000 iterations from the McMC algorithm are plotted. Within these iterations, the Markov chains seem to have reached the same stationary state. Figure 19 shows convergence plots for realizations from the prior pdf $f(\boldsymbol{e})$, using the anisotropic potentials from Simulation 8. Configurations of the favored direction are observed to be more frequently represented in the Markov chain. Also Figure 19 gives an indication of fast convergence.

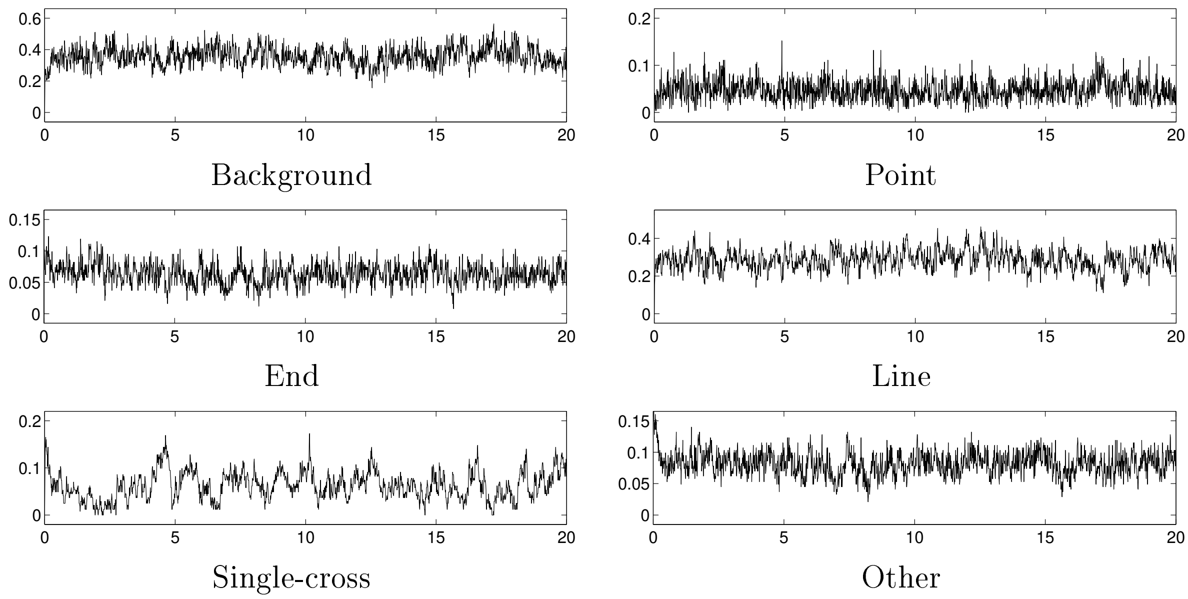

Figure 17: Plots of the relative number of configurations belonging to some of the classes listed in Table 1. The potentials of example 1 in Table 3 are used. The number of iterations is 20 000 and every 10th iteration is plotted. The scale of the horizontal axis is 1000.

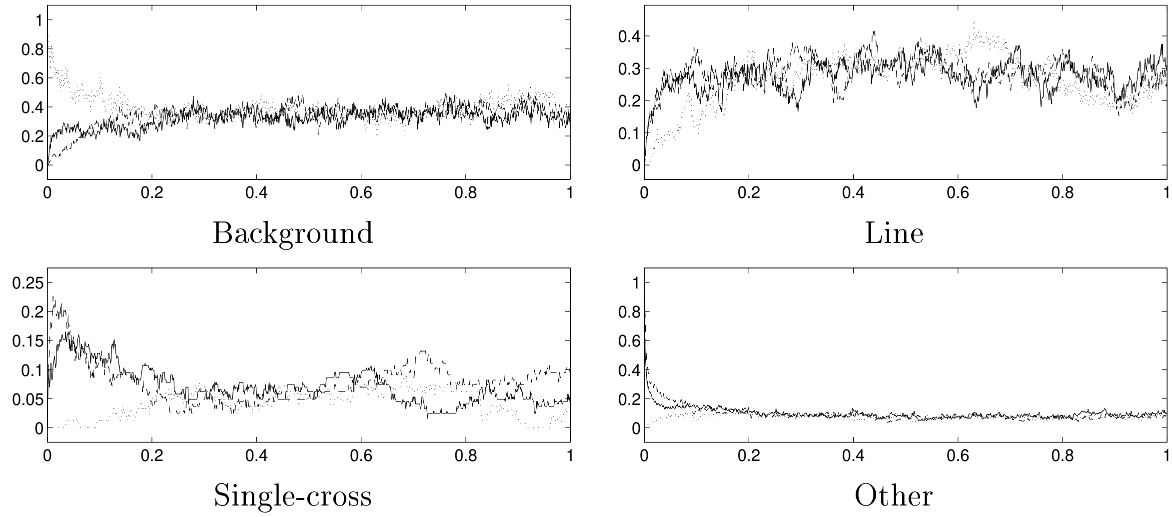

Figure 18: Plots of the relative number of configurations belonging to some of the classes listed in Table 1, using various initial states of the Markov chain. The potentials of example 1 in Table 3 are used. The first 1000 iterations from the prior pdf $f(\boldsymbol{e})$ are plotted, and the scale of the horizontal axis is 1000. Solid lines correspond to initial states where each edge value is drawn at random. Dotted lines show simulations where all edges have initial value $E = 0$, for dashed lines all initial values are $E = 1$.

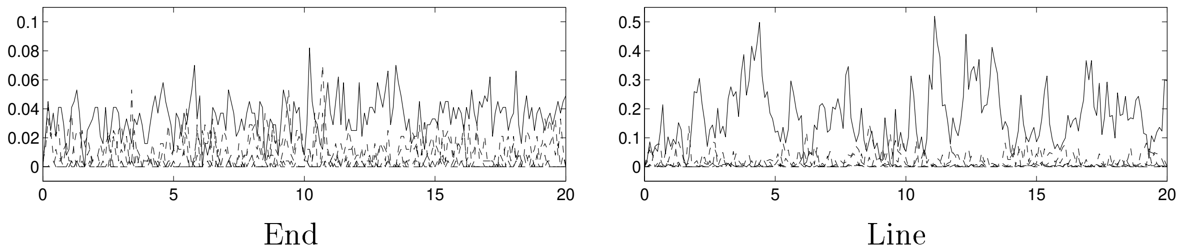

Figure 19: Plots of the relative number of configurations belonging to some of the classes listed in Table 2. The potentials of example 8 in Table 3 are used. The number of iterations is 20 000 and every 10th iteration is plotted. The scale of the horizontal axis is 1000. Solid lines represent configurations belonging to direction 2, the favored direction, while the other are plotted with dashed lines.

8 Simulation Examples using Synthetic Observations

The aim of this work is to generate faulted horizons H conditioned to observations $\boldsymbol{O}$, using the sampling technique described in Section 6. In this section synthetic data is used to study the model and the proposed algorithm. In Section 8.1 the synthetic data is presented, and in Section 8.2 simulation examples from the posterior distribution are studied. In the examples in Section 8.2 a small number of edges, vertices and pixels is chosen, to reduce the dimension of the sample space of the prior distribution.

8.1 Synthetic observations

To generate synthetic observations, data from a non-faulted reservoir is first generated. Reflection coefficients $\boldsymbol{C}_u \sim N(\mu_{c_u}, \Sigma_{c_u})$ of a non-faulted reservoir are drawn from a Gaussian distribution with mean μ_{c_u} and covariance matrix Σ_{c_u}, see Expression (21), using the covariance and correlation function given in Expressions (22) and (23) respectively. The size of the data set is $50 \times 50 \times 20$, and cross sections through the reflection coefficients are shown in Figure 20. The choice of parameter values are inspired by the work of Eide (1999), and are given in Table 5a. Seismic data $\boldsymbol{S}_u^o = A(\psi_s)\boldsymbol{C}_u + \boldsymbol{U}$ of the non-faulted reservoir are obtained by convolution of the reflection coefficients with the Ricker wavelet (20), adding Gaussian noise of mean 0 and variance σ_s^2, see Expression (19). The parameter ψ_s of the Ricker wavelet, the variance and the time step δt are given in Table 5b. Cross sections through the generated seismic data are shown in Figure 21. The generated reflection coefficients $\boldsymbol{C}_u$ and seismic data $\boldsymbol{S}_u^o$ represent the reservoir prior to faulting in the examples below.

A synthetic faulted horizon H is sampled from the prior pdf $f(h)$ in Expression (15), using Algorithm 1, Appendix A. The number of concentric bands of pixels in the hexagonal image is 5. The parameter values used in the prior pdf are given in Table 5c. The the horizon covers a hexagonal area, while the seismic observations are generated over a square area. The square area is placed inside the hexagonal area, and only the part of the horizon where observations are available is illustrated in Figure 22. Seismic data of the faulted reservoir are obtained using Expression (27), $S^o(x, y, t) = S_u^o(x, y, t + H(x, y))$, where $t + H(x, y)$ is rounded off to the closest observation point t_k. The faulted horizon in Figure 22 gives the seismic data shown in Figure 23. Reflection coefficients in four wells are found using Expression (24), $C^o(x, y, t) = C_u(x, y, t + H(x, y))$, and are shown in Figure 24. The well positions are picked at random, and are marked in Figure 23. The complete set of synthetic observations $\boldsymbol{O}$ consists of the seismic data $\boldsymbol{S}^o$ and the reflection coefficients $\boldsymbol{C}^o$.

When the seismic amplitudes $\boldsymbol{S}_u^o$ in Figure 21 are transformed according to Expression (27), columns of the images in Figure 21b-c are shifted up or down, depending on the values of $H(x, y)$. The result of the transformations is a non-rectangular area of observations. To

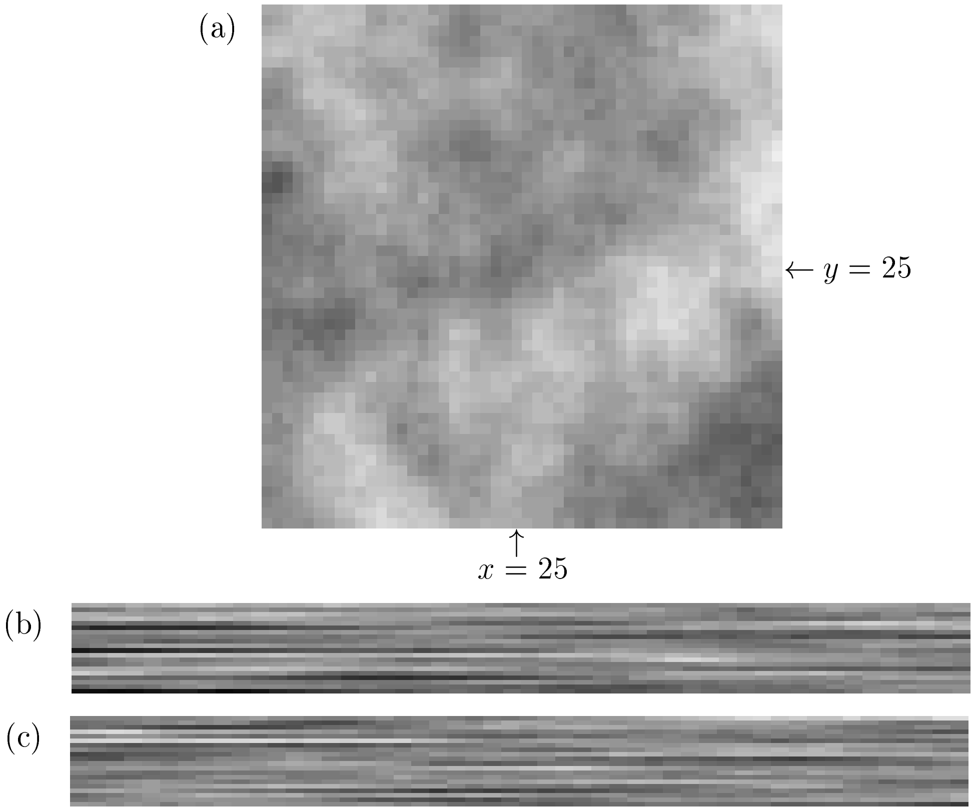

Figure 20: Synthetic reflection coefficients $\boldsymbol{C}_u$ in an unfaulted reservoir. (a) Top horizontal layer. (b) Vertical N-S oriented cross section through the reservoir at position $x = 25$. (c) E-W oriented cross section at $y = 25$. Different horizontal scales are used.

μ_c	σ_c^2	ν	a_H	a_V
0.0	0.035^2	1.2	40	15

(a)

σ_s^2	ν_M	δt
0.0015^2	40	0.002

(b)

$f(\boldsymbol{e})$										$f(\boldsymbol{v}\mid\boldsymbol{e})$		$f(\boldsymbol{p}\mid\boldsymbol{e},\boldsymbol{v})$		
γ_1	γ_2	γ_3	γ_4	γ_5	γ_6	γ_7	γ_8	γ_9	γ_{10}	μ_v	θ	σ_p^2	ν	a
-1.0	0.7	-1.0	0.5	-1.1	0.125	-0.9	-0.8	0.2	2.5	0.01	0.5	0.01^2	2	3

(c)

Table 5: Parameters involved in (a) the Gaussian distribution of reflection coefficients $\boldsymbol{C}_u$ prior to faulting, (b) the relationship between reflection coefficients $\boldsymbol{C}_u$ and seismic data $\boldsymbol{S}_u^o$ and (c) the prior distribution $f(h) = f(\boldsymbol{e})f(\boldsymbol{v}|\boldsymbol{e})f(\boldsymbol{p}|\boldsymbol{e},\boldsymbol{v})$ of the fault pattern H.

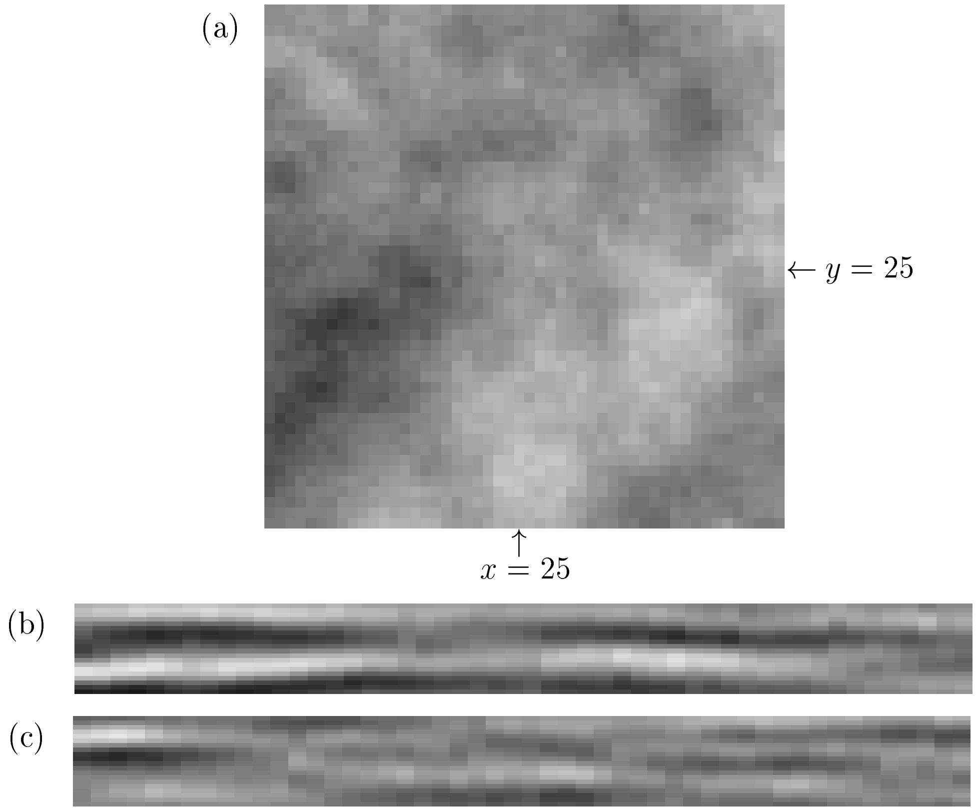

Figure 21: Seismic data $\boldsymbol{S}_u^o$ resulting from a convolution of the reflection coefficients in Figure 20 with the Ricker wavelet, and Gaussian noise added. (a) Top horizontal layer. (b) Vertical N-S oriented cross section through the reservoir at position $x = 25$. (c) E-W oriented cross section at $y = 25$. Different horizontal scales are used.

overcome this problem, only the 8 middle layers of the data set is used, and all shifts are restricted to having maximum size 6. Thus the 8 layers in the middle will always contain data after the transformations, and only these data are used as seismic observations $\boldsymbol{S}^o$. The size of the seismic dataset is thus $50 \times 50 \times 8$. Similar restrictions are used for the observed reflection coefficients from wells. Note that the observation points lying inside this rectangular area after transformation will differ according to the faulted horizon H. In visual representations of the seismic data or well data, all data are included, and the part of a data column that is transformed below the boundary of the image is added on the top, see Figure 23. Similar for data transformed above the image boundary.

Realizations H generated from the posterior distribution of the faulted horizon conditioned to synthetic observations can be compared to the true horizon. Furthermore, given the fault pattern H the observations can be transformed back to their original positions by inverting Expressions (24) and (27). For a given realization of H the transformed seismic data can be compared to the true non-faulted reservoir $\boldsymbol{S}_u^o$ illustrated in Figure 21.

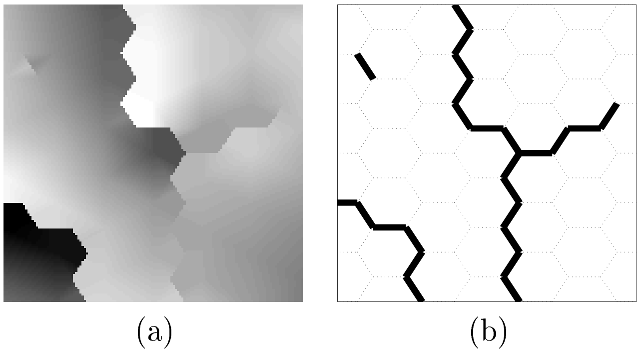

Figure 22: (a) Faulted horizon h from $f(h)$ and (b) corresponding pattern of fault traces $\boldsymbol{e}$.

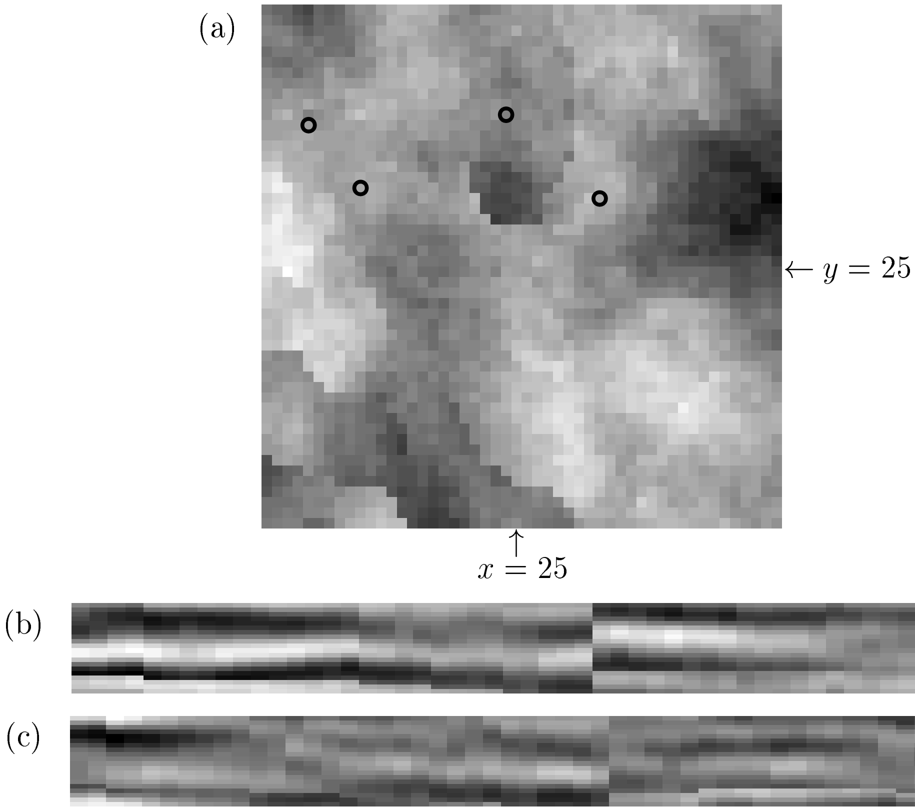

Figure 23: Seismic data $\boldsymbol{S}^o$ after faulting, corresponding to the data in Figure 21. (a) Top horizontal layer, where the circles mark the well positions. (b) Vertical N-S oriented cross section at position $x = 25$. (c) E-W oriented cross section at $y = 25$. Different horizontal scales are used.

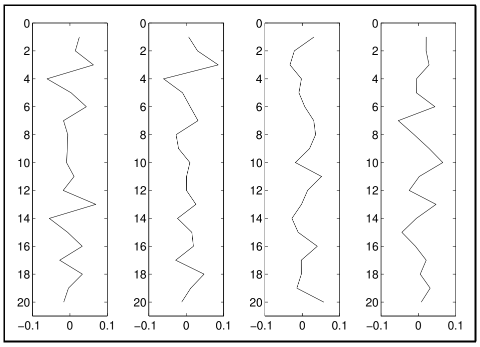

Figure 24: Reflection coefficients $\boldsymbol{c}^o$ obtained in four vertical wells.

8.2 Sampling from the posterior model

The synthetic data from Section 8.1 are used as observations of a faulted reservoir. Figure 25 shows an E-W oriented vertical cross section through the seismic data at position $y = 40$. Based on the observations $\boldsymbol{o} = (\boldsymbol{s}^o, \boldsymbol{c}^o)$, four realizations of the fault pattern in the reservoir are generated from the posterior pdf $f(h|\boldsymbol{o})$, Expression (34). Each realization is generated by restarting the McMC algorithm, thus all samples are independent. 50 000 iterations are run, using an initial burn-in of 5000 for the sampling from $f(\boldsymbol{e})$. In Figure 26 the generated horizons are compared with the true, known faulted horizon. Only the part of the horizons where observations are available is included in the plots. Figure 27 gives a comparison of the true and sampled fault trace pattern on the horizon. One of the main features of the faulted horizon is a N-S striking fault with a relatively large offset in the upper part of the image, see Figure 26. This fault is present in all four realizations. A NW-SE striking fault gives a low altitude of the horizon in the lower left corner of the image. This low-altitude area is also recognized in the realizations, but there is some uncertainty about the orientation of the fault. The lower part of the N-S striking fault and the intersecting fault segment to the right have small offsets, and the realizations of edge images in Figure 27 reveal uncertainties in these areas. However, from Figure 26 the variation of altitude in these areas is observed to be relatively small both for the true faulted horizon and the realizations from the posterior.

In Figure 28 the seismic observations $\boldsymbol{s}^o$ from Figure 25 are transformed back to their

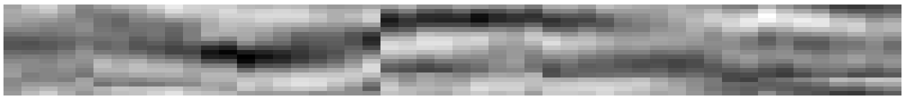

Figure 25: E-W oriented cross section through the seismic observations $\boldsymbol{s}^o$ at position $y = 40$.

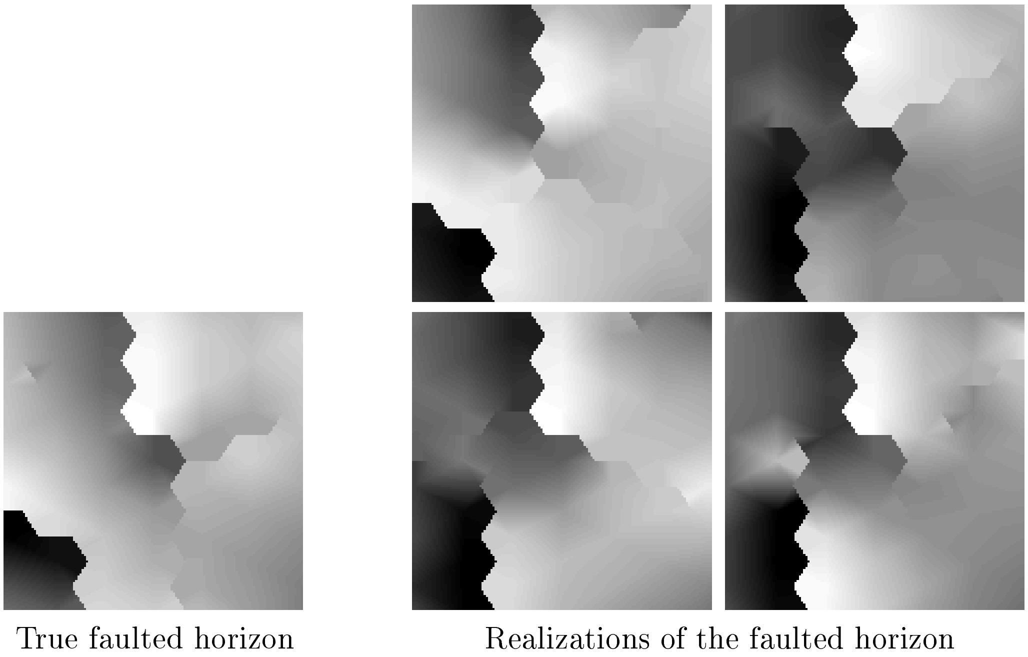

Figure 26: True faulted horizon h compared to four realizations from the posterior pdf $f(h|\boldsymbol{o})$ in Expression (34).

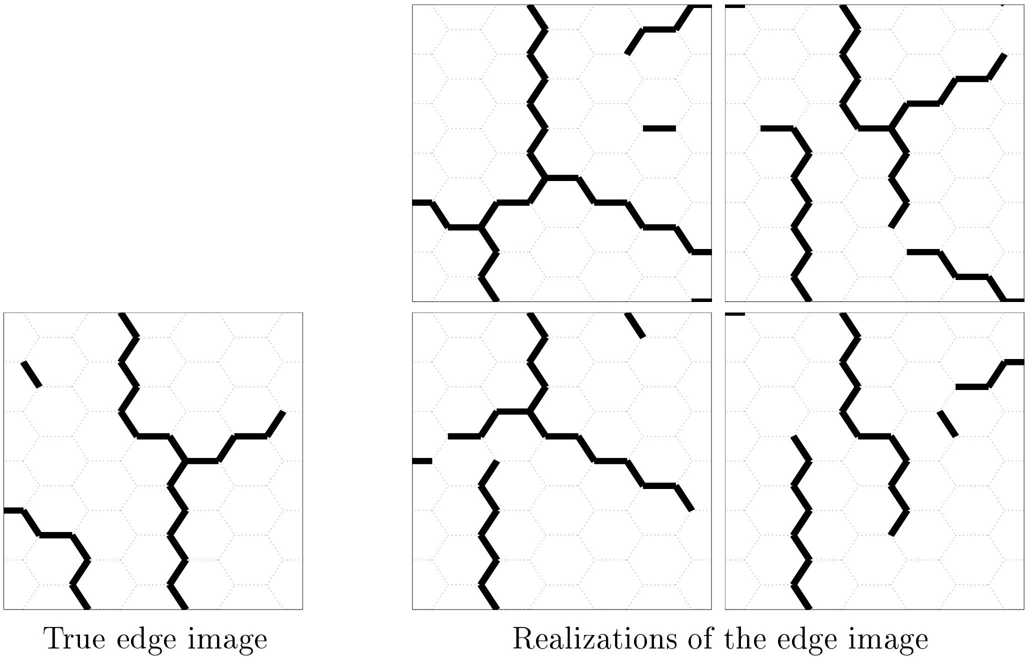

Figure 27: True edge image $\boldsymbol{e}$, representing the pattern of fault traces on the horizon h, compared to the edge images of the realizations shown in Figure 26.

original structure according to the realizations of the faulted horizon in Figure 26, as illustrated in Figure 16. The cross-sections intersect the upper part of the N-S striking fault. This fault can be observed in Figure 25, while it is no longer visible in the transformed observations in Figure 28.

Figure 29a illustrates the variation in sampled offsets along fault traces. For each fault trace falling inside the observation area, the offset is measured at vertices and edge center points along the trace. The offsets of the true faulted horizon are compared to the offsets of the realizations, using different symbols for each realization. Absolute values of the offsets are reported. Fault traces that are present only in the true fault pattern or in a realization appears as points along the axes. The mismatches in Figure 29a mainly originate from the uncertainty around the position and orientation of the NW-SE striking fault in the bottom left corner of the true faulted horizon in Figure 26. This fault has a relatively large offset. Apart from offsets along these fault traces, the bulk of the points in Figure 29a are scattered around the diagonal, indicating a relatively good agreement between offsets along fault traces in the true faulted horizon and the realizations. Figure 29b shows a histogram of offset values in cases where the edge value differs between the true image $\boldsymbol{e}$ and a realization $\boldsymbol{e}_j$, see Figure 27. The figure shows that the amount of misclassified edges decreases as the offset increases, and edges that differ between the true image and a realization have mainly small offsets.

The convergence of the McMC sampling is studied by considering the energy of the likelihood function:

$$U(\boldsymbol{o}|h) = (\boldsymbol{o} - \mu_o(h))'\Sigma_o(h)^{-1}(\boldsymbol{o} - \mu_o(h))/2, \tag{37}$$

where a relatively low energy gives a relatively high likelihood, and vice versa. Figure 30 shows a plot of $U(\boldsymbol{o}|h)$ for the four runs, with accepted proposals of H indicated. It is observed from the figure that the acceptance ratio is very low. This can partly be related to the proposal distribution, which is chosen as the prior pdf. The prior pdf of this high dimensional variable will typically be much more spread out than the posterior pdf, and the proportion of proposals located in the high density area of the posterior is low. For all runs of the algorithm, the plot shows an initial decrease in the energy $U(\boldsymbol{o}|h)$ during the first 20 000 iterations. Later, few new proposals are accepted, and the energy remains low.

Each realization reported above required 1–2 days of simulation, where the McMC algorithm is implemented in the C programming language and was run on a Solaris 2 UNIX work station. As mentioned above, the time consumption of the algorithm is influenced by the time required to span the sample space of H and the time it takes to evaluate the likelihood function at each step of the algorithm. The potential for a speed up of the algorithm lies mainly within the choice of updates in the McMC algorithm and the evaluation of the approximated likelihood function at each step of the algorithm.

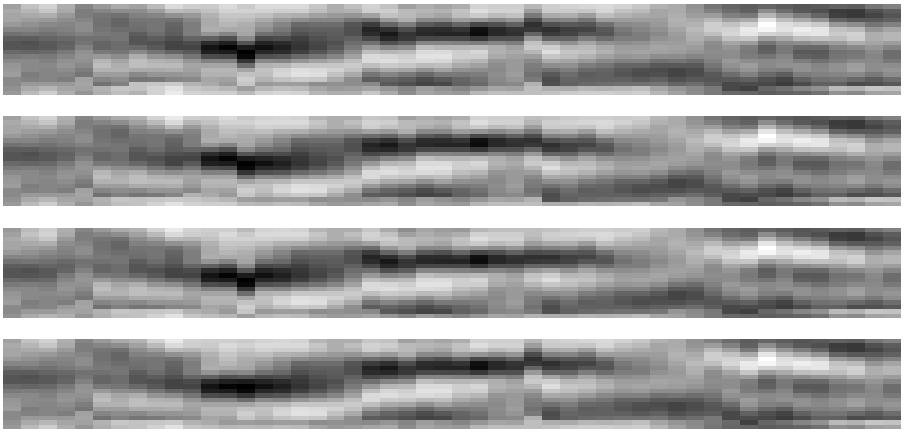

Figure 28: Seismic observations $\boldsymbol{s}^o$ from Figure 25 transformed back to the original structure, according to the realizations of the faulted horizon in Figure 26. The concept of this transformation is illustrated in Figure 16.

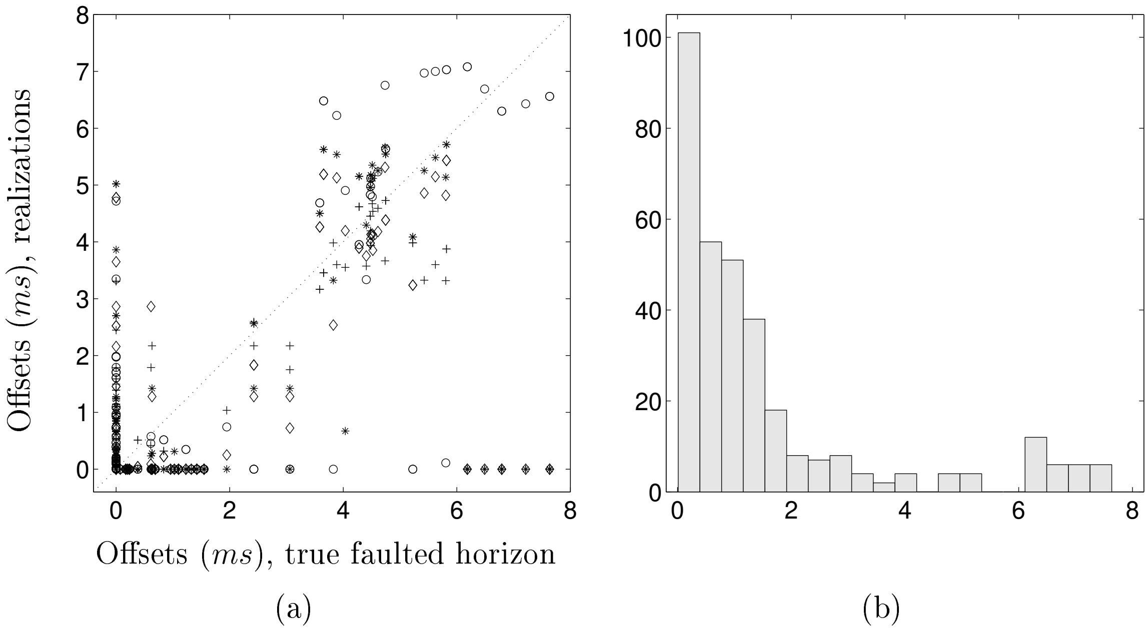

Figure 29: (a) Comparison of offset at vertices and edges for the true faulted horizon and the realizations in Figure 26. Different symbols are used for the four realizations. (b) Histogram of offset values at edges that are misclassified.

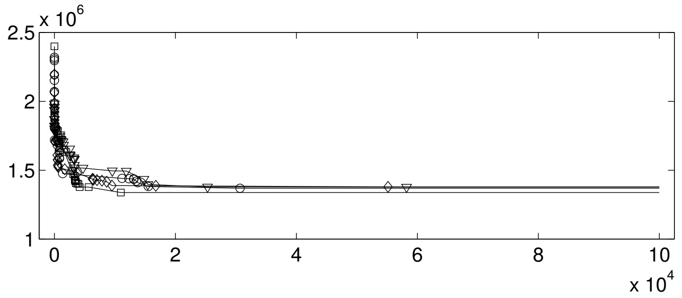

Figure 30: Plots of the energy function $U(\boldsymbol{o}|h)$ in the likelihood function $f(\boldsymbol{o}|h)$, see Expression (37), for the simulations from the posterior pdf. Different symbols ($\square, \diamond, \circ, \triangledown$) are used to mark accepted proposals in each run of the McMC algorithm.

9 Real Data

In this section the stochastic model for fault patterns and the McMC sampling algorithm are applied to a dataset of real seismic observations. Only seismic data are included, since no well observations are available. The location of the seismic survey is confidential. An E-W oriented vertical cross section through the three dimensional seismic cube is presented in Figure 31a, where faults of approximately vertical dip directions are visible. Figure 31b shows a horizontal cross section through the seismic cube. The dataset is considered by geologists to be of good quality.

When the model and the McMC algorithm were first applied to large sections of this dataset, problems were encountered and no satisfactory results were obtained. To be able to investigate the nature of the problems and the limitations of the model and the algorithm, smaller sections of the dataset are studied.

A section of size $8 \times 8 \times 20$ is extracted from the data, see Figure 32, and is used in the stochastic model. The location of the extracted data is indicated in Figure 31, and the dataset is observed to contain at least one fault. Figure 33 shows realizations of the horizon H and the corresponding pattern of fault traces, $\boldsymbol{E}$, sampled from the posterior pdf in Expression (34). The number of concentric bands of pixels in the hexagonal image is 5. The parameter μ_v of the prior pdf $f(\boldsymbol{v}|\boldsymbol{e})$ is chosen as $\mu_v = 0.0025$, the potentials γ_j in the prior pdf $f(\boldsymbol{e})$ are chosen equal to the potentials of example 3 in Table 3, and the remaining variables are chosen as reported in Table 5. The number of iterations is 100 000, using 5000 initial burn-in iterations in the McMC sampling from $f(\boldsymbol{e})$.

All realizations in Figure 33 show a N-S striking fault, with rock on the east side of the fault offset downwards. The realizations reveal some uncertainty in the northern part of the major fault trace and in the pattern of smaller fault traces east and west of the major fault. Figure 34 shows the original structure of the cross section in Figure 32a, obtained based

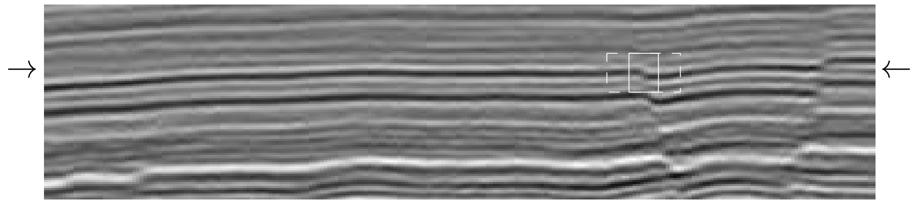

(a)

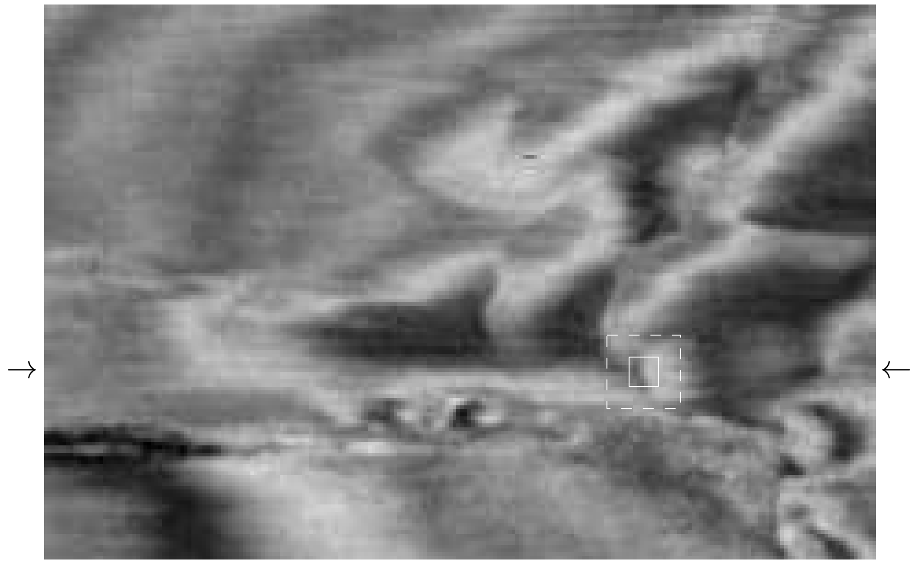

(b)

Figure 31: (a) E-W oriented vertical cross section and (b) horizontal cross section through a three dimensional seismic cube of size $151 \times 226 \times 100$. The arrows mark the positions of the cross sections. The white rectangles mark smaller sections which are extracted and further examined, one of size $8 \times 8 \times 20$ (solid lines) and one of size $20 \times 20 \times 20$ (dashed lines).

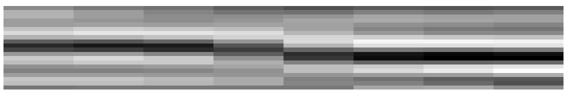

(a)

(b)

Figure 32: (a) E-W oriented vertical cross section and (b) horizontal cross section through a three dimensional seismic cube of size $8 \times 8 \times 20$. The location of the dataset is marked in Figure 31.

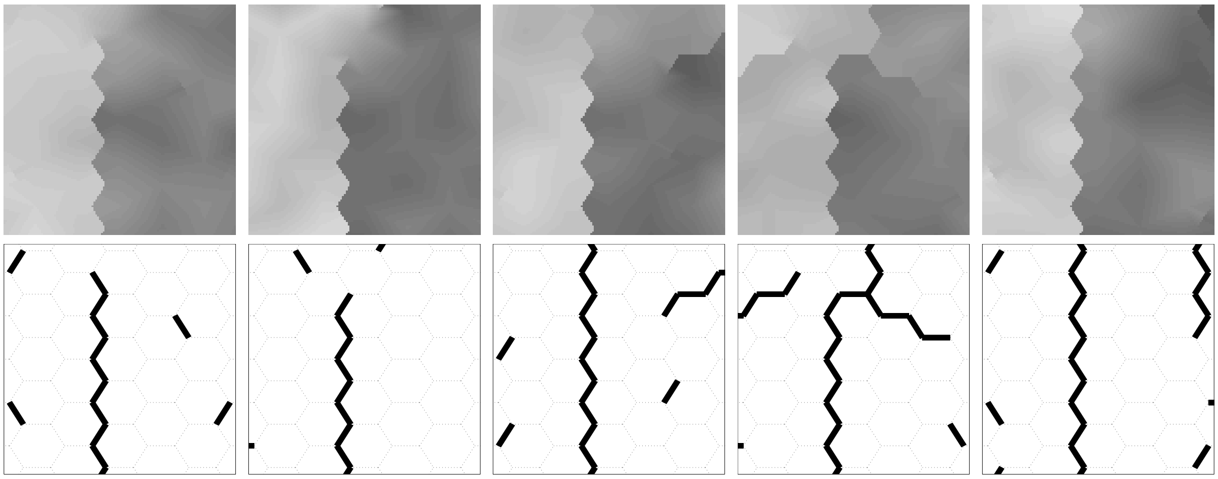

Figure 33: Realizations of H and corresponding $\boldsymbol{E}$, conditioned to a seismic cube of size $8\times8\times20$.

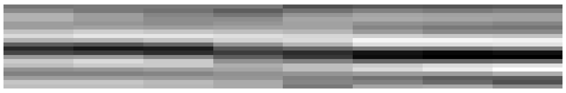

Figure 34: The vertical cross section from Figure 32a after transformation back to the original structure according to one of the realizations in Figure 33.

on one of the realizations of H in Figure 33. The vertically dipping fault in Figure 32a is no longer detectable in Figure 34. The other realizations of H give similar results. Based on the results in Figures 33 and 34, the model and the sampling algorithm are considered to work properly when applied to a small section of seismic data.

The extracted dataset is enlarged horizontally, obtaining a dataset of size $20 \times 20 \times 20$, while the hexagonal image is expanded to 11 bands of pixels. The location of the dataset is marked in Figure 31. Figure 35 shows two realizations of H and the corresponding $\boldsymbol{E}$, using the same model parameters as above and running 50 000 and 500 000 iterations of the McMC algorithm. The time consumption of the latter run was 2-3 days. No common fault traces are observed in the two realizations in Figure 35, and based on the knowledge about the true fault pattern the results of neither run seem reliable. Repeated runs with 50 000 iterations gave similar results, with no common major features in the resulting fault patterns. In general it can be concluded for this dataset that either the model assumptions are not able to reflect the reality, or that 500 000 iterations is not sufficient to give a satisfactory convergence of the McMC algorithm.

Other datasets of sizes ranging from $20 \times 20 \times 20$ to $50 \times 50 \times 20$ were extracted from the seismic cube and used in the stochastic model, and also these gave disappointing results. Most of the McMC runs resulted in horizontal, non-faulted realizations of H, although the

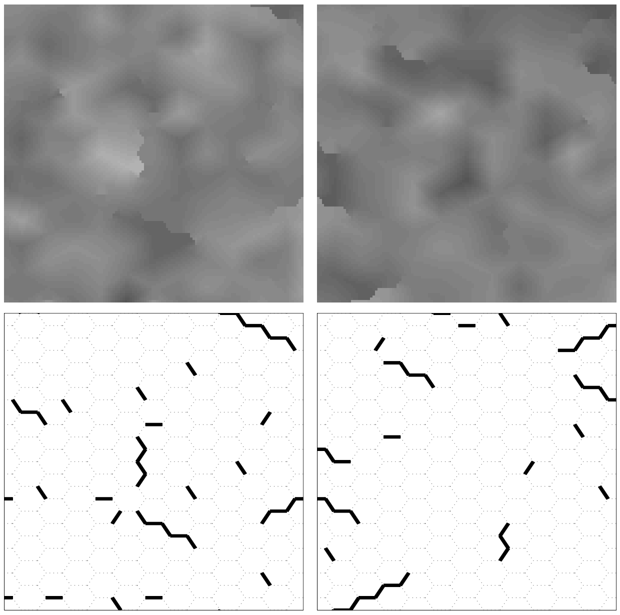

Figure 35: Realizations of H and the corresponding $\boldsymbol{E}$, conditioned to a seismic cube of size $20 \times 20 \times 20$.

datasets were extracted from regions where faults are visible in the seismic data. Relatively coarse grids of 5-7 bands of pixels were used for the hexagonal image.

The examples above show satisfactory results when only a small seismic cube is used in the model, while problems arise when the dataset is enlarged. The main sources of the problems encountered are believed to be restrictive model assumptions and the time consumption of the sampling algorithm. The time consumption of each iteration of the McMC algorithm depends on the grid sizes of both the hexagonal image and the seismic cube, which determines the time required to sample from the prior and to evaluate the likelihood. The model assumptions that are considered to be potential sources of difficulties are:

(i) Faults are vertical with constant offset vertically.
(ii) Fault planes are infinitely thin.
(iii) Offsets are small compared to the thickness of the formation.
(iv) All fault traces follow the edges of the hexagonal grid.
(v) Reflection coefficients and seismic data follow Gaussian distributions.

The mean and variance of the seismic data of a faulted reservoir are obtained under the assumption of vertical fault planes. If this model is applied to datasets with non-vertical fault planes, the mean and variance will not be obtained correctly as the transformation of rock due to faulting is not perfectly modeled. It is observed in Figure 31a that the faults are only approximately vertical and the offset seems to vary somewhat vertically,

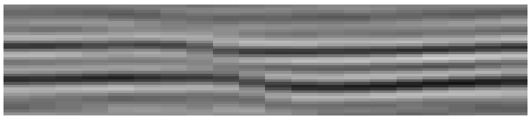

Figure 36: E-W oriented vertical cross section of size 20 (horizontally) $\times$ 40 extracted from the cross section shown in Figure 31a. The cross section covers an enlarged area around the data in Figure 32a.

thus assumption (i) is not completely fulfilled. However, within the extracted dataset in Figure 32a the fault plane is vertical and the offset is constant vertically. Figure 36 shows 20×40 seismic datapoints, where the cross section in Figure 32a is enlarged both horizontally and vertically. From this cross section it is observed that the fault plane does not appear as a vertical, well defined discontinuity, but rather as a dipping band of deformations covering 5-6 observation points horizontally. Thus the figure indicates violations also of assumption (ii). Furthermore, the seismic data close to the fault seem to be somewhat blurred, which may cause slight violations of assumption (v). The blurring is related to the Fresnel zones of the seismic signal, see Sheriff and Geldart (1995). The seismic signal is in practice not reflected from a single point on a reflector, but from a larger area. Close to a fault plane the Fresnel zone will cover areas on both sides of the fault, and the seismic signal from a specific reflector is weakened.

Seismic datasets consisting of 20 datapoints vertically have been used in the examples reported above, corresponding to a thickness of the formation of $40ms$. This vertical thickness enables modeling of faults with vertical offsets up to approximately $20ms$. In the real dataset studied, offset values range from about $4ms$ to beyond $60ms$, thus with seismic cubes of thickness $40ms$ assumption (iii) is not fulfilled by all faults. An example of large offset faults is given in Figure 37. To be able to model the largest fault offsets, seismic cubes of vertical thickness $120 - 150ms$, or 60-75 datapoints, should be used. This magnifies the seismic cube by a factor 3-4 compared to the previous examples, increasing the time required to evaluate the likelihood. Furthermore, the deviations from vertical fault planes become more pronounced when thicker seismic cubes are used.

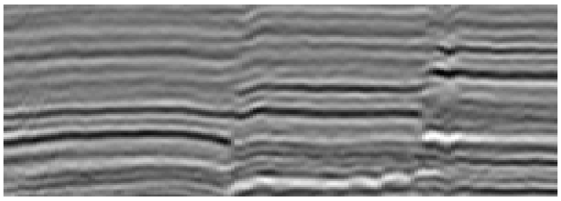

Figure 37: N-S oriented vertical cross section through the three dimensional seismic dataset presented in Figure 31. The two largest faults have offsets of $30 - 50ms$.

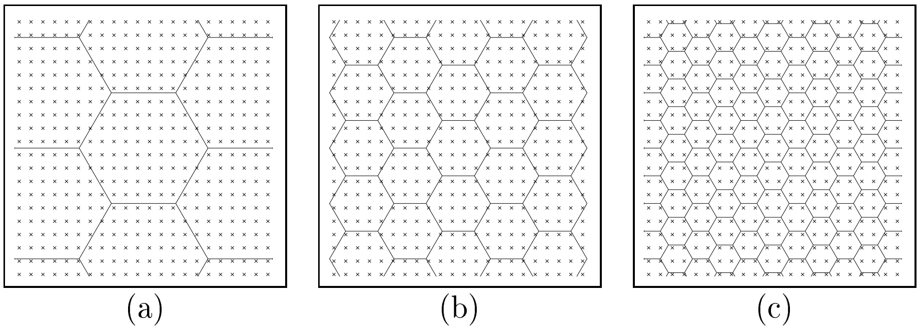

Figure 38: Seismic datapoints (crosses), combined with hexagonal images of gradually finer grids.

Assumption (iv) is obviously not fulfilled by the real dataset. The flexibility in modeling the positions of fault traces relative to the seismic observations depends on the resolution of the hexagonal grid. This is illustrated in Figure 38. The coarse grid in Figure 38a results in large blocks of seismic data inside each hexagonal pixel, with zero probability of any fault traces dividing these seismic datapoints. Figures 38b and 38c show how finer grids can be used to improve the flexibility in the modeling of fault traces. However, refinement of the hexagonal grid implies an enlargement of the sample space of $(\boldsymbol{E}, \boldsymbol{V}, \boldsymbol{P})$, increasing the number of McMC iterations required to span the sample space properly.

A small test is performed aiming at exposing problems related to assumption (v), by investigating the performance of the model and algorithm when assumptions (i)–(iv) are fulfilled. A seismic cube of size $30 \times 30 \times 20$ with no visible faults is used. Two simulation cases are performed, one with the original data and one with a fault pattern sampled from the prior model artificially enforced on the dataset. A hexagonal grid with 5 concentric bands of pixels is used. Simulations based on the original data gave approximately horizontal realizations of H with no faults at seismic scales. When a N-S striking fault was artificially enforced, see Figure 39a, all realizations from the posterior pdf reproduced the fault, see Figure 39b. Based on these examples, no major problems with the Gaussian assumption are apparent.

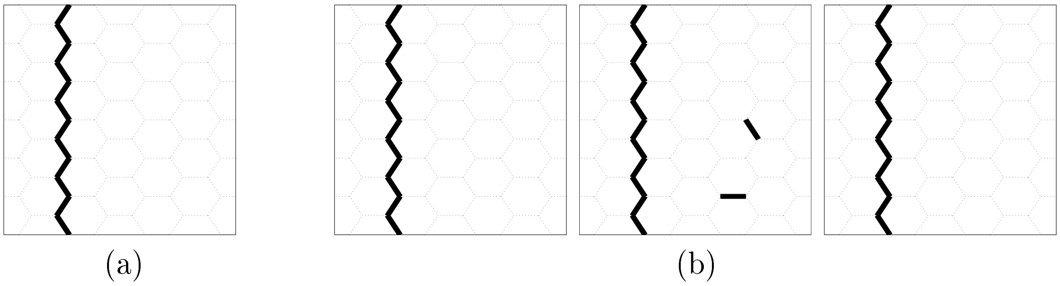

Figure 39: (a) Fault trace artificially enforced on a seismic cube. (b) Realizations from the posterior pdf.

Based on the experience with the real data, it is clear that with the computer power currently available, the performance of the model and the McMC algorithm is of limited value for large real datasets. Model assumptions (iii) and (iv) are related to the time consumption of the McMC algorithm, and problems related to these assumptions could be improved on by increased computer power or more efficient implementation, for example by the use of parallel implementation to evaluate the likelihood function. Violations of assumptions (i) and (ii) can be corrected for by redefining the model to increase flexibility in the modeling of the faults, while assumption (v) is not found to cause any major problems. A possible application for large datasets could be to apply the model to a smaller section within a gliding window. By moving the window across the larger dataset and modeling the fault pattern within a number of smaller sections, the overall fault pattern could be modeled. This could be done either by modeling the fault pattern within each section independently or by including dependencies between the sections, for example modeled through boundary conditions. An alternative approach to dealing with large datasets is to apply a thinning of the seismic data in the horizontal direction. This could improve the fulfillment of assumptions (i) and (ii), and would reduce the size of the seismic cube and thus the time consumption of each McMC iteration. Furthermore, the thinning would have a similar effect on assumption (iv) as the refinement of the grid illustrated in Figure 38. However, the thinning will reduce the seismic resolution horizontally, and can cause problems in distinguishing between fault discontinuities and continuous changes in elevation of comparable magnitude.

10 Conclusion

The paper presents a stochastic model for patterns of faults above seismic resolution, conditioned to three dimensional seismic data and well observations. Based on the typically strong horizontal correlation found in reflection coefficients, and also in seismic data arising from a linear convolution of the reflection coefficients, faults can be recognized as discontinuities in the data.

Due to the complexity of the model, McMC techniques are required to sample from the posterior distribution of fault patterns. The performance of the model and the constructed McMC algorithm is illustrated using a synthetic dataset. In this case the samples from the posterior distribution successfully reproduce the main features of the underlying, known fault pattern.

Problems are encountered when the model and the sampling algorithm are applied to a real seismic dataset, and possible sources of difficulties are discussed. Some of the model assumptions are found not to be completely satisfied. The flexibility of the model is influenced by the resolution of the model, however refinement of the grid is obtained on the expense of the time consumption. Redefinition of the model, increased computer power and more efficient implementation are suggested as improvements of the problems with the model assumptions and resolution. Alternatively, the model and the algorithm can be applied to smaller sections of the data, for example by the use of a gliding window or by thinning of the seismic data.

Acknowledgements

We thank Håkon Tjelmeland for his assistance on this work. Hilde G. Borgos is funded by a PhD grant from VISTA, a research corporation between The Norwegian Academy of Science and Letters and Den norske stats oljeselskap a.s. (Statoil).

References

Abrahamsen, P. (1997). A Review of Gaussian Random Fields and Correlation Functions, *Report 917*, Norwegian Computing Center. Second edition.

Badley, M. E., Freeman, B., Roberts, A. M., Thatcher, J. S., Walsh, J., Watterson, J. and Yielding, G. (1990). Fault Interpretation During Seismic Interpretation and Reservoir Evaluation, *The Integration of Geology, Geophysics, Petrophysics and Petroleum Engineering in Reservoir Delineation, Description and Management*, Proceedings of the 1st Archie Conference, Houston, Texas, pp. 224–241. AAPG.

Bahorich, M. S. and Farmer, S. L. (1995). The coherence cube, *The Leading Edge* **14**(10): 1053–1058.

Bahorich, M. S. and Farmer, S. L. (1996). Method of seismic signal processing and exploration. U. S. Patent Number 5,563,949.

Belfield, W. C. (1998). Incorporating spatial distribution into stochastic modelling of fractures: multifractal and levý-stable statistics, *Journal of Structural Geology* **20**(4): 473–486.

Besag, J. (1974). Spatial Interaction and the Statistical Analysis of Lattice Systems, *J. R. Statist. Soc. B* **36**(2): 192–236.

Besag, J. (1989). Towards Bayesian image analysis, *Journal of Applied Probability* **16**(3): 395–407.

Besag, J., Green, P., Higdon, D. and Mengersen, K. (1995). Bayesian Computation and Stochastic Systems (with discussion), *Statistical Science* **10**(1): 3–66.

Brand, P. J. and Haldorsen, H. H. (1988). Modelling large-scale heterogeneities caused by faulting with a stochastic approach, *Revue de l'Institut français du pétrole* **43**(5): 647–657.

CHILÈS, J. P. (1988). Fractal and Geostatistical Methods for Modeling of a Fracture Network, *Mathematical Geology* **20**(6): 631–654.

CRESSIE, N. A. C. (1993). *Statistics for Spatial Data*, Wiley, New York.

DAWERS, N. H., ANDERS, M. H. AND SCHOLZ, C. H. (1993). Growth of normal faults: Displacement-length scaling, *Geology* **21**: 1107–1110.

EIDE, A. L. (1999). *Stochastic Reservoir Characterization Constrained by Seismic Data*, PhD thesis, Norwegian University of Science and Technology. Doktoringeniøravhandling 1999:5.

EIDE, A. L., OMRE, H. AND URSIN, B. (1997a). Stochastic reservoir characterization conditioned on seismic data, *in* E. Y. Baafi and N. A. Schofield (eds), *Geostatistics Wollongong '96*, Vol. 1, Kluwer Academic Publishers, pp. 442–453.

EIDE, A. L., URSIN, B. AND OMRE, H. (1997b). Stochastic simulation of porosity and acoustic impedance conditioned to seismic data and well data, *67th Annual Meeting of the Society of Exploration Geophysicists, Expanded Abstracts*, SEG, Dallas, Texas.

GAUTHIER, B. D. M. AND LAKE, S. D. (1993). Probabilistic Modeling of Faults Below the Limit of Seismic Resolution in Pelican Field, North Sea, Offshore United Kingdom, *The American Association of Petroleum Geologists Bulletin* **77**(5): 761–777.

GEMAN, S. AND GEMAN, D. (1984). Stochastic Relaxation, Gibbs Distributions, and the Bayesian Restoration of Images, *IEEE Transactions on Pattern Analysis and Machine Intelligence* **6**(6): 721–741.

GRINGARTEN, E. (1996). 3-D Geometric Description of Fractured Reservoirs, *Mathematical Geology* **28**(7): 881–893.

GRINGARTEN, E. (1998). Fracnet: stochastic simulation of fractures in layered systems, *Computers and Geosciences* **24**(8): 729–736.

HASTINGS, W. K. (1970). Monte Carlo sampling methods using Markov chains and their applications, *Biometrica* **57**: 97–109.

LIA, O., OMRE, H., TJELMELAND, H., HOLDEN, L. AND EGELAND, T. (1997). Uncertainties in Reservoir Production Forecasts, *AAPG Bulletin* **81**(5): 775–802.

LUO, Y., HIGGS, W. G. AND KOWALIK, W. S. (1996). Edge detection and stratigraphic analysis using 3d seismic data, *66th Annual Meeting of the Society of Exploration Geophysicists, Expanded Abstracts*, SEG, Denver, Colorado, pp. 324–327.

MARFURT, K. J., KIRLIN, R. L., FARMER, S. L. AND BAHORICH, M. S. (1998). 3-D seismic attributes using a semblance-based coherency algorithm, *Geophysics* **63**(4): 1150–1165.

Marfurt, K. J., Sudhaker, V., Gersztenkorn, A., Crawford, K. D. and Nissen, S. E. (1999). Coherency calculations in the presence of structural dip, *Geophysics* **64**(1): 104–111.

Monroe, J. S. and Wicander, R. (1994). *The Changing Earth*, West Publishing Company.

Munthe, K., Holden, L., Mostad, P. and Townsend, C. (1994). Modelling Sub-seismic Fault Patterns Using a Marked Point Process, *Proceedings of the 4th European conference on the Mathematics of Oil Recovery, Røros, Norway.* Topic B: Heterogeneity Description and Assessment of Uncertainty.

Munthe, K. L., Omre, H., Holden, L., Damsleth, E., Heffer, K., Olsen, T. S. and Watterson, J. (1993). Subseismic Faults in Reservoir Description and Simulation, *68th Annual Conference and Exhibition of the Society of Petroleum Engineers*, Society of Petroleum Engineers, pp. 843–850. SPE Paper 26500.

Omre, H. and Tjelmeland, H. (1997). Petroleum geostatistics, *in* E. Y. Baafi and N. A. Schofield (eds), *Geostatistics Wollongong '96*, Vol. 1, Kluwer Academic Publishers, pp. 41–52.

Ripley, B. D. (1987). *Stochastic Simulation*, Wiley, New York.

Sheriff, R. E. and Geldart, L. P. (1995). *Exploration Seismology*, 2 edn, Cambridge University Press.

Tjelmeland, H. (1996). *Stochastic models in reservoir characterization and Markov random fields for compact objects*, PhD thesis, Norwegian University of Science and Technology. Doktoringeniøravhandling 1996:44.

Tjelmeland, H. and Besag, J. (1998). Markov Random Fields with Higher-Order Interactions, *Scandinavian Journal of Statistics* **25**(3): 415–433.

Todoeschuck, J. P., Jensen, O. G. and Labonte, S. (1990). Gaussian scaling noise model of seismic reflection sequences: Evidence from well logs, *Geophysics* **55**(4): 480–484.

Walsh, J. J. and Watterson, J. (1987). Distribution of cumulative displacement and seismic slip on a single normal fault surface, *Journal of Structural Geology* **9**(8): 1039–1046.

Walsh, J. J. and Watterson, J. (1988). Analysis of the relationship between displacements and dimensions of faults, *Journal of Structural Geology* **10**(3): 239–247.

Wen, R. and Sinding-Larsen, R. (1997). Stochastic modeling and simulation of small faults by marked point processes and kriging, *in* E. Y. Baafi and N. A. Schofield (eds), *Geostatistics Wollongong '96*, Vol. 1, Kluwer Academic Publishers, pp. 398–414.

Winkler, G. (1995). *Image Analysis, Random Fields and Dynamic Monte Carlo Methods*, Springer.

A Sampling Algorithms

A Metropolis-Hastings algorithm is used to sample from the posterior pdf $f(h|\boldsymbol{o})$ of the faulted horizon H conditioned to the observations $\boldsymbol{O}$ of the reservoir. Several alternative transition steps are used, resulting in different transition kernels. The algorithm is given as follows:

Algorithm 1 — Sampling from $f(h|\boldsymbol{o})$

Let n_e, n_v and n_p be the number of edges $\boldsymbol{E}$, vertices $\boldsymbol{V}$ and pixels $\boldsymbol{P}$ respectively, and let $\Omega_e^{n_e}$, $\Omega_v^{n_v}$ and $\Omega_p^{n_p}$ be the sample spaces of $\boldsymbol{E}$, $\boldsymbol{V}$ and $\boldsymbol{P}$. Furthermore, let $\sum_{i=1}^{3} \pi_i = 1$, where $0 \leq \pi_i \leq 1$.

- *Initiate arbitrary $\boldsymbol{e}(0) \in \Omega_e^{n_e}$, $\boldsymbol{v}(0) \in \Omega_v^{n_v}$ and $\boldsymbol{p}(0) \in \Omega_p^{n_p}$,*
  let $h(0) = h(\boldsymbol{e}(0), \boldsymbol{v}(0), \boldsymbol{p}(0))$.
- *Iterate $t = 1, 2, \ldots$*
  - *Let $\boldsymbol{e} = \boldsymbol{e}(t-1)$, $\boldsymbol{v} = \boldsymbol{v}(t-1)$, $\boldsymbol{p} = \boldsymbol{p}(t-1)$ and $h = h(t-1)$.*
  - *Generate $\boldsymbol{e}'$, $\boldsymbol{v}'$ and $\boldsymbol{p}'$ in one of the following ways:*

    (i) *With probability π_1:*
    $$\begin{aligned} &\boldsymbol{e}' \sim f(\boldsymbol{e}') \\ &\boldsymbol{v}' \sim f(\boldsymbol{v}'|\boldsymbol{e}') \\ &\boldsymbol{p}' \sim f(\boldsymbol{p}'|\boldsymbol{e}', \boldsymbol{v}') \\ \textit{hence} \quad &q(h'|h) = f(\boldsymbol{e}') f(\boldsymbol{v}'|\boldsymbol{e}') f(\boldsymbol{p}'|\boldsymbol{e}', \boldsymbol{v}') \end{aligned}$$

    (ii) *With probability π_2:*
    $$\begin{aligned} &\boldsymbol{e}' = \boldsymbol{e} \\ &\boldsymbol{v}' \sim f(\boldsymbol{v}'|\boldsymbol{e}) \\ &\boldsymbol{p}' \sim f(\boldsymbol{p}'|\boldsymbol{e}, \boldsymbol{v}') \\ \textit{hence} \quad &q(h'|h) = f(\boldsymbol{v}'|\boldsymbol{e}) f(\boldsymbol{p}'|\boldsymbol{e}, \boldsymbol{v}') \end{aligned}$$

    (iii) *With probability π_3:*
    $$\begin{aligned} &\boldsymbol{e}' = \boldsymbol{e} \\ &\boldsymbol{v}' = \boldsymbol{v} \\ &\boldsymbol{p}' \sim f(\boldsymbol{p}'|\boldsymbol{e}, \boldsymbol{v}) \\ \textit{hence} \quad &q(h'|h) = f(\boldsymbol{p}'|\boldsymbol{e}, \boldsymbol{v}) \end{aligned}$$
  - *$h' = h'(\boldsymbol{e}', \boldsymbol{v}', \boldsymbol{p}')$.*
  - *With acceptance probability $\alpha(h'|h)$*
    $$\alpha(h'|h) = \min\left\{1,\ \frac{f(\boldsymbol{o}|h')}{f(\boldsymbol{o}|h)}\right\}$$
    let $h(t) = h'$, $\boldsymbol{e}(t) = \boldsymbol{e}'$, $\boldsymbol{v}(t) = \boldsymbol{v}'$ and $\boldsymbol{p}(t) = \boldsymbol{p}'$.
    Otherwise let $h(t) = h$, $\boldsymbol{e}(t) = \boldsymbol{e}$, $\boldsymbol{v}(t) = \boldsymbol{v}$ and $\boldsymbol{p}(t) = \boldsymbol{p}$.

The variable $H(t)$ has pdf $f^t(h|\boldsymbol{o})$ where $\lim_{t\to\infty} f^t(h|\boldsymbol{o}) = f(h|\boldsymbol{o})$.

Algorithm 1 includes steps where realizations are generated from the prior pdfs $f(\boldsymbol{e})$, $f(\boldsymbol{v}|\boldsymbol{e})$ and $f(\boldsymbol{p}|\boldsymbol{e},\boldsymbol{v})$. Exact samples can be drawn from the prior distributions of $\boldsymbol{V}$ and $\boldsymbol{P}$, while McMC techniques are used to generate samples from the prior distribution of $\boldsymbol{E}$. Algorithms 2–4 below describe how samples can be generated from the prior distributions.

The edges $\boldsymbol{E}$ are modeled as a Markov random field, see Section 3.2.1. A sample from the prior pdf $f(\boldsymbol{e})$ of the edges is generated using the following Metropolis-Hastings algorithm:

Algorithm 2 — Sampling from $f(\boldsymbol{e})$

Let n_e be the number of edges in $\boldsymbol{E}$ and $\Omega_e^{n_e}$ the sample space of $\boldsymbol{E}$.

- *Initiate arbitrary $\boldsymbol{e}(0) \in \Omega_e^{n_e}$.*
- *Iterate $t = 1, 2, \ldots$*
  - $\boldsymbol{e} = \boldsymbol{e}(t-1)$.
  - *For $k = 1, 2, \ldots, n_e$*
    - $i \sim \text{Unif}\{1, \ldots, n_e\}$.
    - $e_i' \sim \text{Unif}\{\Omega_e \setminus \{e_i\}\}$, $e_j' = e_j$ *for* $j \neq i$.
    - *Hence* $q(\boldsymbol{e}'|\boldsymbol{e}) = n_e^{-1}(|\Omega_e| - 1)^{-1}$.
    - *With acceptance probability*

$$\alpha(\boldsymbol{e}'|\boldsymbol{e}) = \min\left\{1,\ \exp\{-\sum_{c\in\mathcal{C};i\in c} (\omega_c(\boldsymbol{e}_c') - \omega_c(\boldsymbol{e}_c))\}\right\},$$

      let $e_i = e_i'$, *otherwise retain* e_i.
  - $\boldsymbol{e}(t) = \boldsymbol{e}$.

The edge values $\boldsymbol{E}(t)$ has pdf $f^t(\boldsymbol{e})$ where $\lim_{t\to\infty} f^t(\boldsymbol{e}) = f(\boldsymbol{e})$.

When Algorithm 2 is used within Algorithm 1, burn-in iterations of Algorithm 2 is run before Algorithm 1 is started. When a realization from $f(\boldsymbol{e})$ is needed in update step (i) of Algorithm 1, a limited number of iterations of Algorithm 2 is performed. These iterations of Algorithm 2 are performed to reduce dependency between the samples from $f(\boldsymbol{e})$. Typically, 5–10 000 burn-in iterations of Algorithm 2 are run, while realizations from $f(\boldsymbol{e})$ used in Algorithm 1 are separated by 50 iterations of Algorithm 2.

The prior distribution of the vertices $\boldsymbol{V}$, conditioned on the edges $\boldsymbol{E}$, is a combination of a stochastic offset direction along each fault trace and a deterministic offset profile given the offset direction, see Section 3.2.2. A sample from the prior pdf $f(\boldsymbol{v}|\boldsymbol{e})$ is generated by exact drawing of the offset directions and evaluation of the corresponding offset profiles. The algorithm is given as follows:

Algorithm 3 — Sampling from $f(\boldsymbol{v}|\boldsymbol{e})$

Suppose $\sum_{b_j \in \mathcal{B}_e} |b_j| + |b_0| = n_v$, where n_v is the number of vertices in $\boldsymbol{V}$, b_j is the index set of vertices along fault trace j and $\mathcal{B}_e$ is a partitioning of edges in the realization $\boldsymbol{e}$ into fault traces. The sample space of $\boldsymbol{V}$ is given as $\Omega_v^{n_v} \subseteq \mathbb{R}^{n_v}$.

- *For $i \in b_0$*
  - $V_i = 0$
- *For $b \in \mathcal{B}_e$*
  - $D_b \sim f(d_b)$, *where* $f(1) = \theta$, $f(-1) = 1 - \theta$.
  - $n =$ *length of fault trace* b
  - $i =$ *number of isolated fault tips of* b
  - $\boldsymbol{V}_b = D_b \boldsymbol{g}_{i,n}$

A sample of $\boldsymbol{V}$ from the prior pdf $f(\boldsymbol{v}|\boldsymbol{e})$ is thus obtained. The vectors $\boldsymbol{g}_{i,n}$, $i = 0, 1, 2$, are defined in Section 3.2.2. If there are several possible partitionings of $\boldsymbol{e}$ into fault traces, the set $\mathcal{B}_e$ is picked at random among the $n_b(\boldsymbol{e})$ possibilities. This is done by randomly partitioning each intersection point into a fault tip and an intersected fault trace.

The pixels $\boldsymbol{P}$ are modeled as a multivariate Gaussian distribution conditioned on edges $\boldsymbol{E}$ and vertices $\boldsymbol{V}$, see Section 3.2.3. An exact sample from the prior distribution of the pixels, conditioned on the edges and vertices, is generated in the following way:

Algorithm 4 — Sampling from $f(\boldsymbol{p}|\boldsymbol{e}, \boldsymbol{v})$

Let n_p be the number of pixels in $\boldsymbol{P}$. The prior pdf of pixels, conditioned on edges and vertices, is $f(\boldsymbol{p}|\boldsymbol{e}, \boldsymbol{v}) = \phi(\boldsymbol{p}; \mu(\boldsymbol{e}, \boldsymbol{v}), \Sigma_p)$, and the sample space of $\boldsymbol{P}$ is $\Omega_p^{n_p} \subseteq \mathbb{R}^{n_p}$.

- *Find the matrix $\boldsymbol{A}$ using a Cholesky decomposition of Σ_p: $\Sigma_p = \boldsymbol{A}\boldsymbol{A}'$.*
- *For $i = 1, 2, \ldots, n_p$ generate $Y_i \sim N(0, 1)$.*
- *Let $\boldsymbol{y} = (y_1, y_2, \ldots, y_{n_p})$ and $\boldsymbol{p} = \mu(\boldsymbol{e}, \boldsymbol{v}) + \boldsymbol{A}\boldsymbol{y}$.*

The pixel values $\boldsymbol{p}$ form a sample from the prior pdf $f(\boldsymbol{p}|\boldsymbol{e}, \boldsymbol{v})$. Inversion sampling is used to sample from the standard Gaussian distribution $N(0, 1)$, see Ripley (1987).